ADVANCED ENERGY MATERIALS
www.advenergymat.de

Enhancing Solid Oxide Fuel Cells Development through Bayesian Active Learning

R. K. Jeela, G. Tosato, M. Ahmad, M. Wieler, A. Koeppe, B. Nestler, and D. Schneider**

Ensuring the sustainable operation of solid-oxide fuel cells (SOFCs) requires an understanding of the components' lifespan. Multiphase-field simulation studies play a major role in understanding the underlying microstructural changes and the resulting property alterations in SOFCs over time. The primary challenge in such simulations lies in identifying a suitable model and defining its parametrization. This study presents an Active Learning framework combined with Bayesian Optimization to identify optimal model parameters to simulate the aging of nickel-gadolinium doped ceria (Ni-GDC) anodes. The study overcomes incompleteness and inconsistency of literature data, and navigates the complex, high-dimensional parameter space, by leveraging experimental microstructure data and the power of the AL framework. The successful parameter search enables simulation studies of Ni-GDC anode aging and performance during long-term SOFC operation. This approach improves the accuracy of phase-field simulations and offers a versatile tool for broader applications in SOFC development, predicting material behavior under various operational conditions.

1. Introduction

Solid oxide fuel cells (SOFCs) are prime candidates to replace fossil fuels with a renewable energy source.[1] Their high efficiency in converting fuel into electricity in a clean and sustainable way results in reduced greenhouse gas emissions. Operating at temperatures between 600°C – 900°C, SOFCs are particularly suitable for supplying power to large systems such as data centers or industrial plants, with the added benefit of utilizing waste heat for secondary electricity generation or heat supply. For a sustainable operation of the SOFC, it is of utmost importance to understand the lifespan of its individual components. The basic structure of a fuel cell consists of an anode, a cathode, and an electrolyte. The specific selection of the electrolyte characterizes the fuel cell type, and typically the choice of a solid ceramic inorganic oxide results in a SOFC.[2] A significant challenge in the long-term application of SOFCs is the progressive degradation of their functional materials, primarily attributed to microstructural changes. One key factor contributing to performance degradation is the anode functional layer (AFL), where fuel gas reactions occur.

Nickel-gadolinium doped ceria (Ni-GDC) anodes represent a promising alternative to traditional nickel-yttria stabilized zirconia (Ni-YSZ) anodes, distinguished by the mixed ionic and electronic conductivity of gadolinium-doped ceria (GDC). Research on Ni-ceria SOFC anodes reveals that the major aging phenomenon results from the coarsening, agglomeration, and depletion of nickel,[3,4] as in the case of Ni-zirconia cermets. While the zirconia matrix typically remains stable, notable microstructural changes were identified in GDC within Ni-GDC composites.[3,5–7]

A distinct aging phenomenon in Ni-GDC systems is the formation of GDC coatings on nickel (Ni) particles, observed after approximately 15000 hours of operation in dry conditions and between 1000 and 2300 hours under humid conditions.[3,5] As particles grow, Ni-Ni and Ni-GDC contacts diminish, reducing triple-phase boundary (TPB) density and increasing electronic resistance. Thus, understanding solid oxide cell (SOC) degradation due to microstructural changes is crucial for predicting and improving SOFC lifespan. Alongside experimental investigations, microstructural simulations play a vital role in understanding SOC degradation, reducing time and cost expenditures.

R. K. Jeela, M. Ahmad, B. Nestler, D. Schneider
Institute of Digital Materials Science (IDM)
Karlsruhe University of Applied Sciences
Moltkestraße 30, 76133 Karlsruhe, Germany
E-mail: ravi.jeela@partner.kit.edu; daniel.schneider@kit.edu

G. Tosato, A. Koeppe, B. Nestler, D. Schneider
Institute for Applied Materials-Microstructure Modelling and Simulation (IAM-MMS)
Karlsruhe Institute of Technology (KIT)
Straße am Forum 7, 76131 Karlsruhe, Germany

M. Wieler
Computational Materials Engineering (CR/ATC1)
Robert Bosch GmbH
Robert-Bosch-Campus 1, 71272 Renningen, Germany

B. Nestler, D. Schneider
Institute of Nanotechnology - Microstructure Simulations (INT-MSS)
Karlsruhe Institute of Technology (KIT)
Hermann-von-Helmholtz-Platz 1, 76344 Eggenstein-Leopoldshafen, Germany

The ORCID identification number(s) for the author(s) of this article can be found under https://doi.org/10.1002/aenm.202501216

DOI: 10.1002/aenm.202501216

However, a big challenge for such simulation studies lies in finding a suitable model for coarsening in Ni-GDC anode and defining its parameters.

The phase-field method is used in conjunction with SOFC anodes by several authors.[8–14] In this regard, the model of refs. [15,16] presents a few advantages, as detailed in ref. [16] and briefly summarized in the following. The model enables controlling the interfacial energies independently for each binary interface, concurrently preserving equal and finite interfacial thicknesses, and quantitatively reproducing the interfacial diffusion. In this way, measured surface diffusivities and wetting angles can be accurately incorporated in a straightforward manner. Predicting the long-term degradation of anodes in a quantitative manner requires reliable material parameters under realistic operating conditions, including interface energies and diffusion coefficients. These parameters have a critical role in simulating the coarsening of the Ni-GDC anode. In Section 2.3, a comprehensive review of the literature data for Ni and GDC interface energies and diffusion coefficients is given, highlighting both the scarcity of data and the lack of reliability and accuracy in the reported values, which are required for phase-field simulations. In the work of Hoffrogge et al.,[17] the model is parameterized to describe the coarsening of nickel in Ni-YSZ SOFC anodes at a temperature of $T = 750°C$. The physical parameters were derived from thermal grooving experiments and density functional theory (DFT) calculations.[18,19] Determining experimentally these physical parameters for Ni-GDC anodes at given operating conditions is challenging due to the time-intensive nature of the processes, the significant resources required, the complexity of the measurements, and the associated costs.

As described, Ni-based SOFC anodes exhibit complex changes in their microstructural compositions, which affects the properties of the anodes in a highly non-linear fashion that is difficult to quantify. Interdependencies and correlations between these properties and influencing parameters further complicate the understanding of their behaviors. To investigate this inherent complexity and variability of material properties in SOFCs, automated workflows standardize experimental and numerical studies.[20] Moreover, the integration of machine learning methodologies in those workflows can overcome the resource-intensive nature of those investigations and accelerate fuel-cell research.

The aim of this paper is to enhance SOFCs numerical investigations with Bayesian Active Learning (BAL). Active Learning (AL)[21] is a systematic machine-learning approach to explore vast parameter spaces while minimizing resource expenditures, which, coupled with Bayesian Optimization (BO),[22] emerged as a valuable tool for materials design.[23,24]

Previous works have employed BAL to improve efficiency and reduce experimental time in complex scientific settings. In particle accelerator research and beam optimization, studies by Rousel et al.,[25] and Ji et al.[26] have shown significant improvements in experimental efficiency. Rahmanian et al.[27] performed a one-shot AL with Bayesian hyperparameter tuning to optimize battery electrolyte conductivity. Similarly, Günay and Tapan[28] leveraged a Bayesian optimization loop to reach optimum performance of polymer electrolyte membrane electrolyzer with minimum effort or the minimum number of experiments or observations. In diagnostics, Tapan[29] applied BO with Gaussian process regression to quantify SARS-CoV-2 electrochemical sensor response characteristics. Zhao et al.[30] combined BAL with Variational Autoencoder (VAE) to solve the inverse design problem of process–structure linkage for porous materials. BAL suitability for iterative adaptive design workflows has been further demonstrated in diverse fields, from lattice structures[31] to solid-state electrolytes for lithium-ion batteries.[32] Furthermore, previous work has shown that the method's high adaptability extends to the choice of surrogate models: Lei et al.[33] presented a BO workflow that replaces GP-based surrogate methods with Bayesian multivariate adaptive regression splines (BMARS) and Bayesian additive regression trees (BART). The rapidly evolving field of Large Language Models (LLMs) is also engaging with BAL. Recent work of Melo et al.[34] has extended the method to preference modeling in LLMs, addressing the challenge of efficient data selection for acquiring human feedback.

In this work, we extend and adapt our Computational Intelligence and Data Science (CIDS) framework[35] to incorporate an AL Oracle, which serves as the decision-making component in phase-field simulation workflows. The Oracle guides the learning process by selecting the most informative data points to evaluate, effectively balancing the exploration of the parameter space with the exploitation of known information. This existing knowledge and uncertainty within the problem domain is quantified through Bayesian Optimization employing a probabilistic regression model. Incorporating BO in our design-of-experiments methodology enables effective data-driven material design, significantly reducing the need for resource-intensive simulations while maximizing the value of each evaluation.

To streamline the process, we employed automated workflows within the Kadi4Mat[36] infrastructure, ensuring standardized and sustainable research data management (RDM). This automation facilitates seamless execution and documentation of simulations, enhancing the reproducibility of the results and long-term data sustainability across iterative design processes. We will demonstrate the application of the AL framework to the parameterization of Ni-GDC under the given operating conditions of an SOFC anode. By using pristine and aged Focused Ion Beam Scanning Electron Microscope (FIB-SEM) 3D-reconstructed microstructures coupled with phase-field simulations, we showcase the framework's efficiency in parameter discovery. This application illustrates the potential for broader use of our framework for SOFC development and optimization, as well as for similar numerical and experimental studies.

2. Method

In this section, we present the comprehensive methodology employed to model and simulate the coarsening behavior of Ni-GDC anodes in SOFCs. We begin by detailing the acquisition of 3D microstructure data from Ni-GDC anode samples, followed by an explanation of the phase-field model formulation used for computing coarsening phenomena. Subsequently, we discuss the challenges in determining physical parameters for Ni-GDC anodes model parameterization and review the available literature data. The digital representation of microstructures, together with simulation data of aging processes, sets the stage for our novel AL framework, which efficiently leverages BO to parameterize SOFC simulations and is developed in the form of automated workflows within the Kadi4Mat infrastructure,

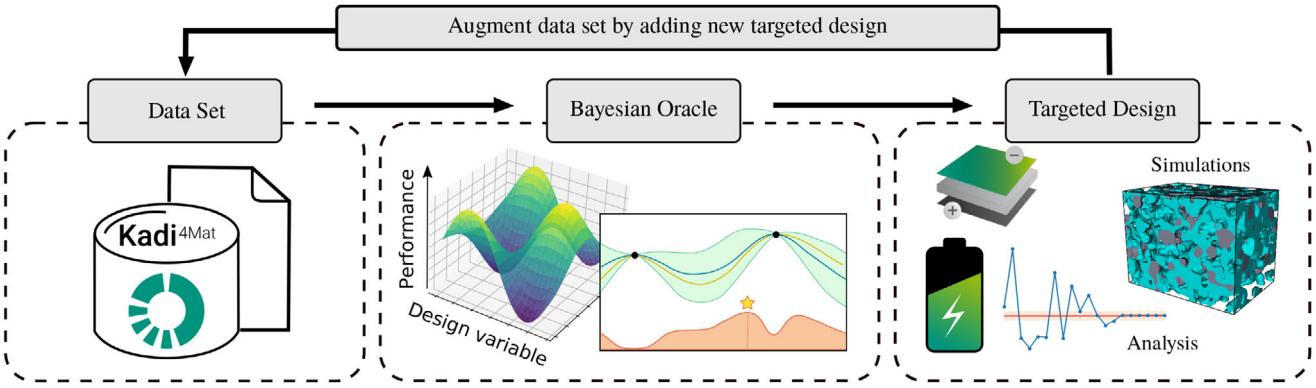

Figure 1. AL framework embedded in SOFCs studies. The whole data process operates within the Kadi4Mat ecosystem, leveraging and expanding its functionalities. The dataset of available SOFC simulations is stored in Kadi4Mat, where it is accessed by the BO Oracle. Using the collected information, the oracle iteratively selects the parameter configurations expected to yield the most informative results for the chosen optimization objective. A simulation is run with each selected configuration, analyzed, scored, and uploaded again into Kadi4Mat, to enrich the data pool guiding the search more effectively.

allowing for seamless data management and iterative optimization. **Figure 1** illustrates the concept and data workflow of the presented AL framework applied to SOFC studies. The requirements for the parameter search, as well as all available SOFC simulations, are stored in Kadi4Mat. Based on these data, the BO Oracle iteratively selects parameter configurations predicted to yield the most informative insights for the optimization objective. Each selected configuration is then simulated, analyzed, scored, and uploaded to Kadi4Mat, incrementally enriching the dataset to enhance the search process.

2.1. Acquisition of 3D Microstructure Data

The 3D microstructure data for this study were reconstructed from small samples of Ni-GDC anodes that were manufactured at Forschungszentrum Jülich (FZJ) and artificially aged at KIT by Y. Liu et al.[6] The samples were analyzed with a Plasma-FIB device, comprising the following steps: (i) infiltration of the pores with an electrically conductive epoxy resin and metallographic sectioning, (ii) micro-preparation with a focused ion beam (FIB), (iii) alternating SEM imaging and slicing with a Plasma-FIB device. The resulting 3D grayscale image was denoised using split-Bregman optimization and then segmented with the watershed algorithm. To find good markers (seeds) for the watershed, a custom procedure was developed that automatically determines suitable thresholds from the gray value histogram and removes all markers near interfaces (large gray value gradient) and near ridge-like features (Meijering filter).

2.2. Pace3D - Parallel Algorithms for Crystal Evolution in 3D

A Multiphase-field Model, based on the grand-potential functional developed by Choudhury and Nestler,[15] is employed with a recent enhancement that accounts for surface self-diffusion[16] to model the coarsening phenomena of both nickel and GDC. The formulation of the model involves the grand-potential functional Ω (in J) of the system of volume V, which is dependent on the order parameters $\boldsymbol{\phi} = \{\phi_\alpha, \phi_\beta, \dots, \phi_N\}$ (dimensionless) of N phases, as well as the volumetric chemical potentials $\boldsymbol{\mu} = \{\mu_1, \mu_2, \dots, \mu_{K-1}\}$ (in Jm^{-3}) of K components, and is stated as:

$$\Omega(\boldsymbol{\phi}, \nabla\boldsymbol{\phi}, \boldsymbol{\mu}) = \int_V \frac{1}{\epsilon} w(\boldsymbol{\phi}) + \epsilon a(\nabla\boldsymbol{\phi}) + \psi(\boldsymbol{\phi}, \boldsymbol{\mu}) \; \mathrm{d}V \tag{1}$$

In this framework, $w(\boldsymbol{\phi})$ (in Jm^{-2}), $a(\nabla\boldsymbol{\phi})$ (in Jm^{-4}) and $\psi(\boldsymbol{\phi}, \boldsymbol{\mu})$ denote the potential, gradient, and bulk terms respectively. The scalar parameter ϵ (in m) controls the length scale and determines the width of the diffuse interface $\delta = \epsilon\pi^2/4$. The combined potential and gradient terms following the notation of ref. [37] incorporate interfacial energy into the model and stabilize the interface profile with finite thickness. The gradient term is given following[38] as:

$$a(\nabla\boldsymbol{\phi}) = -\sum_{\substack{\alpha,\beta=1 \\ \alpha<\beta}}^{N,N} \gamma_{\alpha\beta} \nabla\phi_\alpha \cdot \nabla\phi_\beta \tag{2}$$

where $\gamma_{\alpha\beta}$ (in Jm^{-2}) denotes the interfacial energy of α and β phases. For the present work, we chose an obstacle potential of the form,

$$w(\boldsymbol{\phi}) = \begin{cases} \frac{16}{\pi^2} \sum_{\substack{\alpha,\beta=1 \\ \alpha<\beta}}^{N,N} \gamma_{\alpha\beta}\phi_\alpha\phi_\beta, & \boldsymbol{\phi} \in \mathcal{G} \\ \infty, & \boldsymbol{\phi} \notin \mathcal{G} \end{cases} \tag{3}$$

with Gibbs simplex $\mathcal{G} = \left\{ \sum_{\alpha=1}^{N} \phi_\alpha = 1 : \{\phi_\alpha \geq 0, \forall\alpha \in \{1, \dots, N\}\} \right\}$. The bulk grand-potential density is defined as an interpolation of the grand-potential densities of the bulk phases, given by $\psi(\boldsymbol{\phi}, \boldsymbol{\mu}) = \sum_{\alpha=1}^{N} \psi^\alpha(\boldsymbol{\mu}) h_\alpha(\boldsymbol{\phi})$, where $\psi^\alpha(\boldsymbol{\mu}) = f^\alpha\left(\boldsymbol{c}^\alpha(\boldsymbol{\mu})\right) - \sum_{i=1}^{K-1} \mu_i c_i^\alpha(\boldsymbol{\mu}), \; \forall\alpha \in \{1, \dots, N\}$ represents the grand-potential density for phase α. This incorporates into the functional the bulk free-energy f^α, dependent on the phase-inherent compositions $\boldsymbol{c}^\alpha = \left\{c_1^\alpha, c_2^\alpha, \dots, c_{K-1}^\alpha\right\}$. In the present work, the interpolation function is chosen as $h_\alpha(\boldsymbol{\phi}) = \phi_\alpha$ and satisfies the constraint $\sum_{\alpha=1}^{N} h_\alpha(\boldsymbol{\phi}) = 1$. A local quasi-equilibrium is

assumed, ensuring that at every spatial position, the condition $\mu_i = {}^{\partial f^{\alpha}(c^{\alpha})}/_{\partial c_i^{\alpha}} = {}^{\partial f^{\beta}(c^{\beta})}/_{\partial c_i^{\beta}} = \cdots = {}^{\partial f^{N}(c^{N})}/_{\partial c_i^{N}}$ is satisfied for all $i \in \{1, \ldots, K-1\}$.

The evolution equation of each phase-field ϕ_α, in accordance with,[38] is expressed as:

$$\epsilon \frac{\partial \phi_\alpha(x,t)}{\partial t} = \frac{1}{\tilde{N}} \sum_{\substack{\beta=1 \\ \beta \neq \alpha}}^{N} m_{\alpha\beta} \left(\frac{\delta \Omega}{\delta \phi_\beta} - \frac{\delta \Omega}{\delta \phi_\alpha} \right) \tag{4}$$

Here, $\tilde{N}$ represents the local number of phases, while $m_{\alpha\beta}$ (with units of $m^4/J/s$) denotes the mobility of the interface between phases α and β. The term $\delta/\left(\delta\phi_\alpha\right)$ is the variational derivative with respect to ϕ_α. Nickel and GDC are modeled as pure solids with nearly fixed compositions by introducing free energies of the form $f^{\alpha}\left(\boldsymbol{c}^{\alpha}(\boldsymbol{\mu})\right) = \sum_{i=1}^{K-1} f_i^{\alpha}\left(c_i^{\alpha}\right)$. The individual contributions are assumed to be simple parabolas, specifically $f_i^{\alpha}\left(c_i^{\alpha}\right) = A_i \left(c_i^{\alpha}\left(\mu_i\right) - c_{i,\mathrm{eq}}^{\alpha} \right)^2$, $i \in \{\mathrm{Ni}, \mathrm{GDC}\}$. Here, the prefactor A_i indicates the strength of immiscibility and is set high enough to ensure volume conservation for each phase.

The porous Ni-GDC system is modeled using three distinct order parameters $\boldsymbol{\phi} = \{\phi_{\mathrm{Ni}}, \phi_{GDC}, \phi_{Pore}\}$, representing the metallic nickel phase, the GDC structure and the voids. To enable species transport of each substance, a set of two dimensionless composition variables $\boldsymbol{c} = \{c_{\mathrm{Ni}}, c_{\mathrm{GDC}}\}$ (mole fractions), i.e. $K = 3$, and the porous phase composition as $c_{\mathrm{Pore}} = 1 - \sum_{i=1}^{K-1} c_i = 1 - c_{\mathrm{Ni}} - c_{\mathrm{GDC}}$ are employed. The dimensionless composition fields $c_i = \sum_{\alpha=1}^{N} h_\alpha c_i^{\alpha}$ (mole fractions) are conserved quantities. They evolve according to the conservation laws governing the system, as:

$$\frac{\partial c_i(\boldsymbol{x},t)}{\partial t} = -\boldsymbol{\nabla} \cdot \boldsymbol{j}_i \tag{5}$$

where $\boldsymbol{j}_i$ denotes the flux of species i (in ms^{-1}). The evolution of the chemical potential is represented in Einstein's notation as:

$$\frac{\partial \mu_i(\boldsymbol{x},t)}{\partial t} = \left[\sum_{\alpha=1}^{N} h_\alpha(\boldsymbol{\phi}) \frac{\partial c_j^{\alpha}(\boldsymbol{\mu})}{\partial \mu_i} \right]^{-1} \left[\frac{\partial c_j(\boldsymbol{x},t)}{\partial t} - \sum_{\alpha=1}^{N} c_j^{\alpha}(\boldsymbol{\mu}) \frac{\partial h_\alpha(\boldsymbol{\phi}(\boldsymbol{x},t))}{\partial t} \right] \tag{6}$$

For SOFC anodes, Surface diffusion is assumed to be the primary mechanism for mass transfer in the typical operating temperature range of the SOFC. Compared to the Ni-YSZ anodes, the Ni-GDC anodes exhibit both nickel and GDC evolution over time.[39] In addition to the diffusion of nickel and GDC species along the surfaces, the diffusion along the Nickel/GDC interface is also considered in this model. By accounting for diffusion pathways beyond the surface, the model provides a more comprehensive understanding of mass transfer in these anodes. As a result, the flux density of nickel is expressed as:

$$j_{\mathrm{Ni}} = -\frac{32}{\pi^2 \epsilon} \nabla \mu_{\mathrm{Ni}} \left(M_{\mathrm{Ni}}^{NiPore} \phi_{Ni} \phi_{Pore} + M_{\mathrm{Ni}}^{NiGDC} \phi_{Ni} \phi_{GDC} \right) \tag{7}$$

The diffusion of nickel along the tangential direction of the free nickel surface and Ni-GDC interface is controlled by the mobilities M_{Ni}^{NiPore} and M_{Ni}^{NiGDC} (units of $m^6/J/s$) respectively. These mobilities are linked to the surface self-diffusivity D_{Ni}^{NiPore} and interface self-diffusivity D_{Ni}^{NiGDC} through an Einstein-like relation (cf. [[16], Eq. (99)]), given by,

$$M_{\mathrm{Ni}}^{NiPore} = \frac{D_{\mathrm{Ni}}^{NiPore} \delta_s V_m \left(\Delta c_{\mathrm{Ni},eq}^{Ni-Pore} \right)^2}{RT} \tag{8}$$

$$M_{\mathrm{Ni}}^{NiGDC} = \frac{D_{\mathrm{Ni}}^{NiGDC} \delta_I V_m \left(\Delta c_{\mathrm{Ni},eq}^{Ni-GDC} \right)^2}{RT} \tag{9}$$

Here, δ_s and δ_I denote the atomistic thickness of the surface and interface respectively (in order of 0.1 nm), V_m is the molar volume of nickel, R and T are the ideal gas constant and temperature, respectively. As $D_{\mathrm{Ni}}^{NiPore}\delta_s$ and $D_{\mathrm{Ni}}^{NiGDC}\delta_I$ enter the above equations, the excess surface diffusivity $D_{\mathrm{Ni,ex}}^{NiPore} \equiv D_{\mathrm{Ni}}^{NiPore}\delta_s$, as well as the excess interface diffusivity $D_{\mathrm{Ni,ex}}^{NiGDC} \equiv D_{\mathrm{Ni}}^{NiGDC}\delta_I$ (in $m^3\ s^{-1}$) are defined. These definitions remove the need to assume the surface and interface thicknesses arbitrarily. The composition difference specific to the model $\Delta c_{\mathrm{Ni},eq}^{Ni-Pore}$ and $\Delta c_{\mathrm{Ni},eq}^{Ni-GDC}$ are defined as $\Delta c_{\mathrm{Ni},eq}^{Ni-Pore} \equiv c_{\mathrm{Ni,eq}}^{Ni} - c_{\mathrm{Ni,eq}}^{Pore} = 0.8$ and $\Delta c_{\mathrm{Ni},eq}^{Ni-GDC} \equiv c_{\mathrm{Ni,eq}}^{Ni} - c_{\mathrm{Ni,eq}}^{GDC} = 0.8$, respectively. Similarly, the flux density of GDC and the associated mobilities are represented as:

$$j_{\mathrm{GDC}} = -\frac{32}{\pi^2 \epsilon} \nabla \mu_{\mathrm{GDC}} \left(M_{\mathrm{GDC}}^{GDCPore} \phi_{GDC} \phi_{Pore} + M_{\mathrm{GDC}}^{NiGDC} \phi_{GDC} \phi_{Ni} \right) \tag{10}$$

$$M_{\mathrm{GDC}}^{GDCPore} = \frac{D_{\mathrm{GDC}}^{GDCPore} \delta_s V_m \left(\Delta c_{\mathrm{GDC},eq}^{GDC-Pore} \right)^2}{RT} \tag{11}$$

$$M_{\mathrm{GDC}}^{NiGDC} = \frac{D_{\mathrm{GDC}}^{NiGDC} \delta_I V_m \left(\Delta c_{\mathrm{GDC},eq}^{Ni-GDC} \right)^2}{RT} \tag{12}$$

Zero flux boundary conditions are enforced at the domain boundaries, treating the boundaries as isolating (i.e., $\boldsymbol{j}_i \cdot \boldsymbol{n} = 0 \forall i, x \in dV$), where $\boldsymbol{n}$ denotes the normal to the domain boundary, indicating no net flux across the boundary. Additionally, a perpendicular contact condition is assumed for the order parameters ($\boldsymbol{\nabla}\phi_\alpha \cdot \boldsymbol{n} = 0$), ensuring that the gradient of the order parameter is normal to the boundary. This manuscript employs a SIMD-vectorized solver, with the implementation detailed in ref. [40], Sec. 4.2]. For model validation, the interested reader is directed to refs. [16] and [17].

2.3. Physical Parameters and Model Parameterization

This section explains the method for determining the physical parameters for coarsening in the Ni-GDC anode. For the present work, the temperature $T = 900°C$ is chosen, corresponding to the experimental conditions for Ni-GDC anode annealing. Determining the parameters in physical modeling simulations corresponding to experimental conditions is pivotal to quantitatively reproducing the microstructural aging of the Ni-GDC anode as observed in experiments. **Figure 2** demonstrates the importance of identifying these parameters for predicting the long-term performance of the anode under specific operating conditions. For the sake of simplicity, the phase-field model parameters are expressed in a model-specific unit system, with

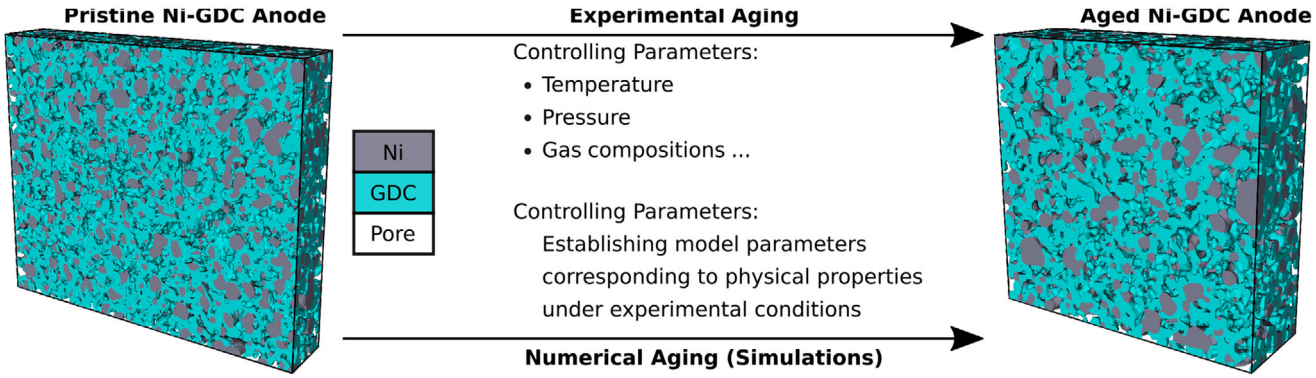

Figure 2. Microstructural evolution in Ni-GDC anodes. Experimental conditions (temperature, environment) drive microstructure changes, while precise parameter settings in physical modeling simulations aim to reproduce these outcomes accurately. This precision is crucial for quantitatively simulating microstructural aging. Note: Size variations between pristine and aged samples reflect different FIB-SEM volume segments, not aging effects.

u_l, u_E and u_t representing the model's units for length, energy, and time, respectively. The length unit u_l is defined based on the resolution of the initial microstructure (Δx) in the numerical grid of discretization $\Delta x = \Delta y = \Delta z$. The energy and time units are related through the Nickel surface energy γ_{NiPore}, Nickel surface diffusivity D_{Ni}^{NiPore}, and temperature T (refer to Equation (8)). **Table 1** presents the model's parameterization.

2.3.1. Nickel Diffusion Coefficients

The mechanisms of volume self-diffusion are well-established, and the corresponding Arrhenius parameters are known with high precision. In contrast, surface diffusion is less extensively studied and exhibits a considerable degree of measurement uncertainty, often varying by one to two orders of magnitude. This variability is evident in the literature, where reported values for surface and grain boundary self-diffusion are highly inconsistent.[41–44] Anisotropy, annealing atmosphere, and material purity significantly influence measured diffusivities. The annealing atmosphere has a particularly pronounced effect on surface diffusion, as the mobility of surface atoms is highly sensitive to the adsorption of gas molecules and impurities. For nickel, the partial pressure of oxygen in the annealing environment notably impacts surface diffusion rates. The current literature on nickel surface and grain boundary diffusion lacks the necessary precision for reliable phase-field simulations. Haremski et al.[19] recently performed thermal grooving experiments on nickel

Table 1. Phase-field parameters used in simulations of Ni-GDC anode. The model units are stated as $u_l = 50$ nm, $u_E = 6.25 \times 10^{-15}$ J, $u_t = 1.45 \times 10^{-2}$ s.

Parameter [symbol]	Value [model units]	Value [physical units]
Ni-surf. chem. mobility (M_{Ni}^{NiPore})	$(10^{-1} \dots 10^{-3})\ u_l^6/(u_E u_t)$	$(1.73 \times 10^{-29} \dots 1.73 \times 10^{-31})$ m^6/J/s
Ni-nickel/GDC interf. chem. mobility (M_{Ni}^{NiGDC})	$(10^{-3} \dots 10^{-8})\ u_l^6/(u_E u_t)$	$(1.73 \times 10^{-31} \dots 1.73 \times 10^{-36})$ m^6/J/s
GDC-surf. chem. mobility ($M_{\mathrm{GDC}}^{GDCPore}$)	$(2.11 \times 10^{-6} \dots 2.11 \times 10^{-9})\ u_l^6/(u_E u_t)$	$(3.65 \times 10^{-34} \dots 3.65 \times 10^{-37})$ m^6/J/s
GDC-nickel/GDC interf. chem. mobility (M_{GDC}^{NiGDC})	$(2.11 \times 10^{-8} \dots 2.11 \times 10^{-14})\ u_l^6/(u_E u_t)$	$(3.65 \times 10^{-36} \dots 3.65 \times 10^{-42})$ m^6/J/s
Interfacial energy Ni-Pore (γ_{NiPore})	$1.0 \dots 0.6\ u_E/u_l^2$	$2.5 \dots 1.5$ J m^{-2}
Interfacial energy Ni-GDC (γ_{NiGDC})	$1.2 \dots 0.4\ u_E/u_l^2$	$3.0 \dots 1.0$ J m^{-2}
Interfacial energy Pore-GDC ($\gamma_{GDCPore}$)	$0.8 \dots 0.28\ u_E/u_l^2$	$2.0 \dots 0.7$ J m^{-2}
Interface mobility Ni-Pore (m_{NiPore})	$(10^{-1} \dots 10^{-3})\ u_l^4/(u_E u_t)$	$(6.92 \times 10^{-15} \dots 6.92 \times 10^{-17})$ m^4/J/s
Interface mobility Ni-GDC (m_{NiGDC})	$(10^{-1} \dots 10^{-3})\ u_l^4/(u_E u_t)$	$(6.92 \times 10^{-15} \dots 6.92 \times 10^{-17})$ m^4/J/s
Interface mobility Pore-GDC ($m_{GDCPore}$)	$(10^{-1} \dots 10^{-3})\ u_l^4/(u_E u_t)$	$(6.92 \times 10^{-15} \dots 6.92 \times 10^{-17})$ m^4/J/s
Interface width parameter (ϵ)	$2.0\ u_l$	100 nm
Voxel-size ($\Delta x = \Delta y = \Delta z$)	$1.0\ u_l$	50 nm
Thermodynamic prefactor Nickel (A_{Ni})	$5\ u_E/u_l^3$	2.5×10^8 J/m^3
Thermodynamic prefactor GDC (A_{GDC})	$50\ u_E/u_l^3$	2.5×10^9 J/m^3
Equil.-comp. Ni-Ni ($c_{\mathrm{Ni,eq}}^{Ni}$)	0.9	90 mol%
Equil.-comp. Ni-GDC ($c_{\mathrm{Ni,eq}}^{GDC}$)	0.1	10 mol%
Equil.-comp. Ni-Pore ($c_{\mathrm{Ni,eq}}^{Pore}$)	0.1	10 mol%
Equil.-comp. GDC-Ni ($c_{\mathrm{GDC,eq}}^{Ni}$)	0.1	10 mol%
Equil.-comp. GDC-GDC ($c_{\mathrm{GDC,eq}}^{GDC}$)	0.9	90 mol%
Equil.-comp. GDC-Pore ($c_{\mathrm{GDC,eq}}^{Pore}$)	0.1	10 mol%

bicrystals to determine the surface diffusion coefficient with high accuracy. These studies, conducted at a temperature of $T = 750°C$, report values that align with those found by Blakely et al.[41] when extrapolating the Arrhenius lines for the {100} and {111} surfaces to lower temperatures. Based on this correlation, the excess surface diffusion coefficient ($D_{Ni,ex}^{NiPore}$) for pure and impure nickel at $T = 900°C$ was evaluated using the Arrhenius equation fitted to Blakely et al.'s experimental data,[41] resulting in a range of 1.74×10^{-21} to 2.1×10^{-20} $m^3\ s^{-1}$. Hoffrogge et al.[17] assumed, following the results of Haremski et al.,[19] that diffusion along the slow {100} surface orientation is rate-limiting and estimated an excess surface diffusion coefficient from an average of four data points near {100} as 3.75×10^{-22} $m^3\ s^{-1}$ at $T = 750°C$. Given the considerable variation in reported surface diffusion values in the literature, excess surface diffusion coefficient with a range of 4.0×10^{-22} $m^3\ s^{-1}$ to 4.0×10^{-20} $m^3\ s^{-1}$ is considered. The diffusion values range considered in this manuscript's study accounts for inherent uncertainties and encompasses both faster and slower diffusion rates along different surface orientations. This approach ensures a comprehensive evaluation of diffusion behavior across various conditions. Due to the scarcity of literature data, the excess diffusion coefficient of nickel along the nickel-GDC interface ($D_{Ni,ex}^{NiGDC}$) is assumed to range from 4.0×10^{-22} $m^3\ s^{-1}$ to 4.0×10^{-27} $m^3\ s^{-1}$. This range is consistent with the general theory that surface diffusion is the fastest, followed by interface diffusion, and bulk diffusion is the slowest.

2.3.2. Nickel Surface Energy

The literature reports experimentally determined mean surface energies of nickel ranging from 1.6 to 2.5 J/m^2, varying with method, temperature, and atmospheric conditions, providing an initial indication of their magnitude.[42,45–49] Complementary to these experimental findings, atomistic simulations can determine the anisotropy of surface energy, typically calculated at $T = 0$ K. It is observed that surface energy decreases with increasing temperature, with a difference of approximately 10% between values at $T = 0$ K and the melting temperature. These simulations have provided weighted mean surface energy values for nickel of 2.04 J/m^2[50] and 2.54 J/m^2,[51] respectively. However, the experimental conditions differ significantly from those within an SOFC anode. Furthermore, the influence of humidity on these parameters has not been extensively studied. It is known that oxygen adsorption can reduce surface energy, and impurities adsorbed on the surface can similarly affect surface energy.

Haremski et al.[18] conducted thermal grooving experiments on Ni polycrystals and Ni-YSZ anode microstructures under SOFC anode operating conditions at $T = 750°C$ in both dry and humid forming gas using atomic force microscopy. The carrier gas used was forming gas ($95\%N_2/5\%H_2$), and a maximum humid atmosphere (29 vol.% H_2O and 71 vol.% forming gas) was chosen, without annealing in an oxidizing environment. The measured oxygen partial pressure was $PO_2 = 10^{-25}$atm in dry forming gas and $PO_2 = 10^{-19}$atm in humid forming gas. They concluded that these values are still low and not forming an oxidizing atmosphere, thus avoiding the adsorption of oxygen on the surface, which could reduce the surface energy.

In the current study, the SOFC operating conditions are at a temperature of $T = 900°C$ with a gas composition of H_2-50% / H_2O-50%, and the material system is Ni-GDC. Under these conditions, the oxygen partial pressure could potentially impact the surface energy values. It was shown in the study by Fujimatsu et al.[52] that the oxygen partial pressure in SOFCs can vary significantly depending on current density, flow rate, and operating temperature and can range up to $PO_2 = 10^{-15}$atm. Also, investigations on the effects of oxygen partial pressure on surface energies indicate that the surface energy decreases with increasing oxygen partial pressure.[53,54] As a result, rather than employing a fixed surface energy value, this study considers the surface energy of nickel as a variable, spanning a range from 1.5 to 2.5 J/m^2, to account for possible variations.

2.3.3. GDC Diffusion Coefficients and Surface Energy

Experimental studies of grain-boundary grooving on polished surfaces of Ceria (CeO_2) annealed in an argon atmosphere were conducted over a temperature range of $1473 - 1773$ K. From Arrhenius plots of the surface diffusion coefficient, the value at $T = 900°C$ was estimated to be $7.2 \times 10^{-18} m^2/s$ and the corresponding excess surface diffusion coefficient as $2.4 \times 10^{-27} m^3/s$.[55] Another study examined polycrystalline CeO_2 by developing thermal grain boundary grooves at different temperatures $1473 - 1663$ K in air, using atomic force microscopy (AFM). The surface diffusion coefficient of CeO_2 was calculated from Arrhenius plots at $T = 900°C$, yielding values ranging from 10^{-18} to $10^{-20} m^2/s$.[56] As a result, GDC excess surface diffusion coefficient ($D_{GDC,ex}^{GDCPore}$) for the AL Bayesian framework is given in the range of 2.4×10^{-25} $m^3\ s^{-1}$ to 2.4×10^{-28} $m^3\ s^{-1}$. Given the lack of experimental data, the excess diffusion coefficient of GDC at the nickel/GDC interface ($D_{GDC,ex}^{NiGDC}$) is assumed to fall within the range of $2.4 \times 10^{-27} m^3 s^{-1}$ to $2.4 \times 10^{-33} m^3 s^{-1}$.

From the literature, it was found that the surface energies of CeO_2 from simulation studies are reported for the {100}, {110}, and {111} surfaces with values of (1.44, 1.06 and 0.71 J/m^2), (1.4, 1.0 and 0.7 J/m^2), and (1.41, 1.04 and 0.69 J/m^2), respectively.[57–59] The GDC surface energy for the {100}, {110}, and {111} surfaces was given as 1.46, 0.90 and 0.74 J/m^2 respectively,[57] Whereas, experimental studies using the multiphase equilibration technique estimated the surface energy of CeO_2 in an argon atmosphere at $T = 900°C$ by extrapolation to be 1.80 J/m^2.[55] Considering all the above findings, the GDC surface energy for the AL Bayesian framework is assigned in the range of 0.7 to 2.0 J/m^2.

2.3.4. Nickel-GDC Interfacial Energy

There is no available literature on interface energies for the Ni-GDC or Ni-CeO_2 systems. However, a study using the multiphase equilibration technique to determine the interface energy of the CeO_2-Cu system in an argon atmosphere at temperatures ranging from $1473 - 1773$ K reports interface energy of 2.88 J/m^2 at $T = 900°C$, based on linear temperature extrapolation.[55] Additionally, various experimental and computational methods have determined the interfacial energy values

for the Ni-YSZ (nickel/yttria-stabilized zirconia) interface. Using Transmission Electron Microscopy (TEM) and Winterbottom analysis, a study measured the interfacial energy for Ni-YSZ(111) in the range of 1.8 to 2.1 J/m^2, depending on the specific configuration of the interface, for Ni-YSZ(001) as around 2.5 J/m^2 at 1350°C in an Ar+H_2 (99%) atmosphere with a PO_2 of 10^{-20} atm.[60,61] By considering these similar systems and to account for different scenarios of wetting to dewetting, a range of 1.0 to 3.0 J/m^2 as Ni-GDC interfacial energy is considered appropriate for this study.

2.3.5. Interface Mobilities and Parabolic Free Energy

A comprehensive investigation of surface diffusion-driven thermal grooving was conducted by Hoffrogge et al.[16] to validate the model employed in the present study against established theories. Their results showed good agreement with analytical solutions of sharp interfaces, confirming model accuracy. In addition, the surface diffusion-controlled kinetics can be correctly quantified using the growth rate constant (B) of the model obtained from the asymptotic analysis. The value of B is evaluated in the present study according to (cf. [[16], Eq. (99) ff.]). In order to minimize the effects of attachment kinetics, the interface mobilities ($m_{\alpha\beta}$) are chosen in this work such that attachment kinetics remain subdominant. It is ensured by the characteristic length scale associated with the attachment kinetics, defined as ($l_c = \sqrt{B/(\gamma_{\alpha\beta}\, m_{\alpha\beta})}$) being much smaller than the diffuse interface width, i.e., ($l_c \ll \pi^2\epsilon/4$).[16]

The minima of the parabolic free energy $c^{\alpha}_{i,\,\mathrm{eq}}$ are specifically chosen values of 0.1 and 0.9, with an emphasis on maintaining adequately distinct values to enable differentiation, for instance, between Ni-rich and Ni-poor phases. The parabolic free energy function's chosen prefactor A_i ensures consistent volume preservation. To establish the model's energy and time scales, we consider the maximum values of nickel's surface diffusion and surface energy. Subsequently, all other model parameters and their respective ranges are aligned with this scaling system. Parameters such as interface mobilities, stable time steps, and simulation time are selected by our AL Bayesian Oracle for each simulation trial. This optimization ensures efficient resource utilization while maintaining a consistent physical time across all simulations.

2.4. Analysis of 3D Ni-GDC Anode Porous Microstructure

The microstructural parameters of the 3D Ni-GDC porous anode–phase volume fraction, specific surface areas, median particle diameter from the continuous particle size distribution, tortuosity, and triple-phase boundary lengths (TPBs)–were precisely calculated using established methods (see **Table B1** in B). These parameters collectively define the anode's structural and functional efficiency, significantly influencing its electrochemical activity, as well as ion and gas transport, and ultimately impacting the overall cell performance.

The continuous particle size distributions, according to Münch and Holzer,[62] are employed to quantify particle sizes during coarsening by measuring the relative volume of a phase that can be filled with overlapping spheres of varying diameters, avoiding artificial segmentation and providing a complementary cumulative distribution that decreases from unity to zero as sphere diameter increases. The median particle size (d_{50}) is determined at the distribution's midpoint value of 0.5. The tortuosity (τ_α) of a phase, a dimensionless number, is estimated by solving the Laplace equation for electric potential under specific boundary conditions, calculated as the ratio of hypothetical ideal current to actual current, providing a scale-invariant geometrical measure of transport pathway complexity.[63] The mean tortuosity is calculated by averaging the values in the x, y, and z directions, i.e., $\tau_\alpha \equiv \frac{1}{3}\left(\tau_{\alpha,x} + \tau_{\alpha,y} + \tau_{\alpha,z}\right)$, which reflects the overall transport characteristics of the phase. The TPB is calculated using a skeletonization algorithm that marks intersection voxels, reduces them to single-voxel thickness, and smooths the network to minimize discretization effects.[64] Specific areas of each phase (A_α) are calculated by integrating the magnitude of its order parameter, i.e., $A_\alpha = \frac{1}{V}\int_V \left|\nabla\phi_\alpha\right| dV$, with individual interface areas ($A_{\alpha-\beta}$) derived by solving a system of linear equations. Given the mixed conductivity of GDC, its entire surface is active for electrochemical reactions, making the interface area of GDC-Pore (forming the double phase boundary, DPB) significant. All these methods were implemented in-house within the PACE3D Framework and validated against known test cases.[17]

Table B1. Microstructural characteristic properties of pristine and 240-hour-aged Ni-GDC anodes.

Parameter	Symbol	Pristine	240h aged
Ni Vol%	V_{Ni}	22.44	22.43
GDC Vol%	V_{GDC}	41.38	39.84
Pore Vol%	V_{Pore}	36.18	37.74
Ni/Pore Specific Area (μm^{-1})	$A_{\mathrm{Ni-Pore}}$	0.37	0.33
GDC/Pore Specific Area (μm^{-1})	$A_{\mathrm{GDC-Pore}}$	1.50	1.38
Ni/GDC Specific Area (μm^{-1})	$A_{\mathrm{Ni-GDC}}$	0.67	0.61
GDC Tortuosity (–)	τ_{GDC}	2.57	3.07
Pore Tortuosity (–)	τ_{Pore}	2.57	2.40
Total TPB density (μm^{-2})	l_{TPB}	1.82	1.55
Nickel Avg. Particle Diameter (μm)	d_{Nickel}	0.91	1.04
GDC Avg. Particle Diameter (μm)	d_{GDC}	0.59	0.62
Pore Avg. Particle Diameter (μm)	d_{Pore}	0.60	0.68
Total volume (μm^3)	V	6666	4800
Voxel size (μm)	$\Delta x = \Delta y = \Delta z$	0.05	0.05

2.5. Subdomains of 3D Microstructure for AL Framework

The size of representative volume elements (RVE) for Ni-GDC anodes is crucial for performing ML-based phase-field simulations. To analyze the RVE size, subdomains representing 1/4th, 1/9th, and 1/16th of the real domain volume were extracted and evaluated. Specifically, subdomain sizes of 14 × 18.5 × 6.4 μm^3 (1/4th of the real domain volume), 9.4 × 12.4 × 6.4 μm^3 (1/9th of the real domain volume), and 7.0 × 9.2 × 6.4 μm^3 (1/16th of the real domain volume) were extracted from the real Ni-GDC anode microstructure (28.2 x 37 x 6.4 μm^3). These subdomains were analyzed and compared based on their microstructural properties to

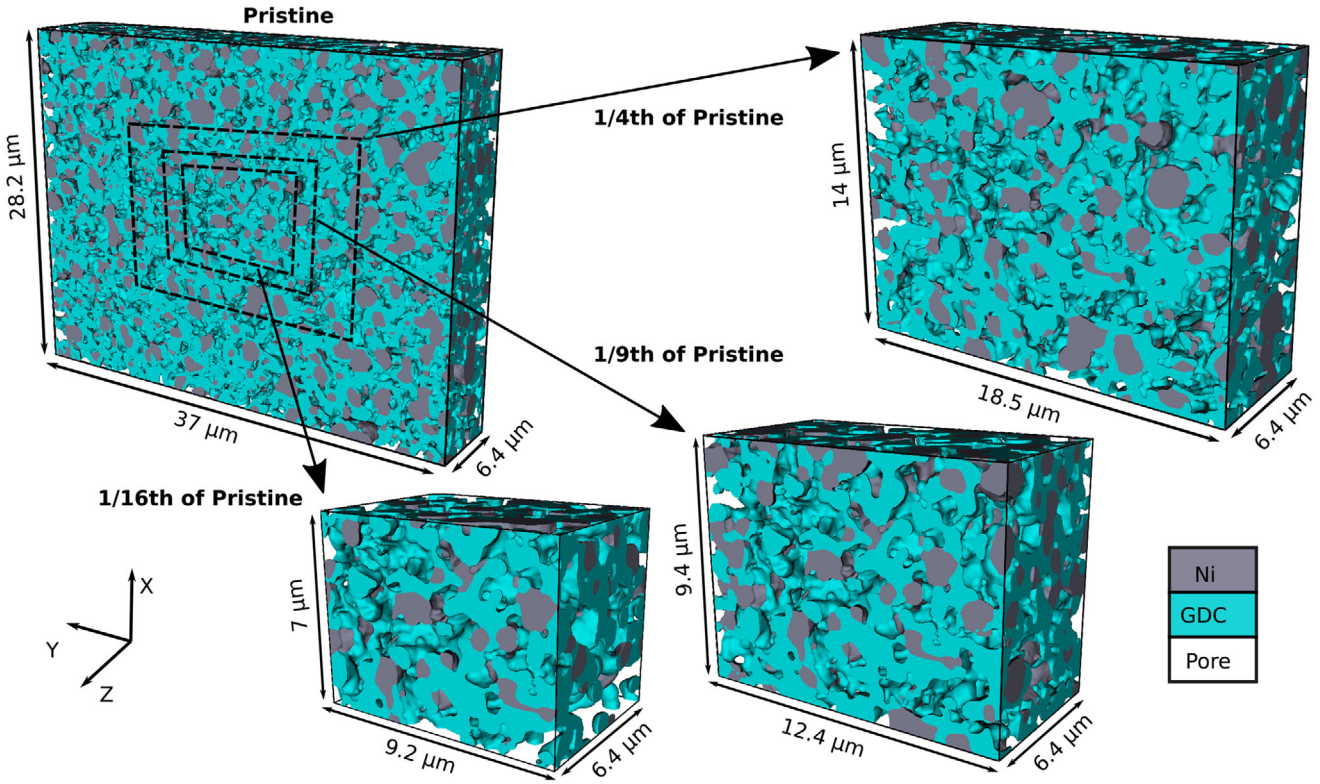

Figure 3. Sub-regions extracted from a pristine FIB-SEM 3D reconstructed real microstructure. Sub-regions representing 1/4th, 1/9th, and 1/16th of the total volume were extracted from the Central region of the real microstructure. Given that the microstructure's thickness in the z-direction is only 6.4 µm, it was kept consistent for all sub-regions, with only x- and y-dimensions being reduced accordingly.

determine the optimal domain size for phase-field simulations. The intention of this paper is to conduct numerous ML-driven phase-field simulations on the initial microstructure, exploring a wide range of thermophysical parameters from the literature to identify the appropriate and missing physical parameters of the Ni-GDC anode under given operating conditions. Although simulating significantly larger volumes could provide comprehensive insights, the requirement for computing resources and simulation times increase greatly. Therefore, the study focuses on finding a balance between computational feasibility and the accuracy of microstructural representation. **Figure 3** illustrates the positions of the subdomains derived from the digital representation of the real microstructure domain and their morphology.

Table B2 in B presents the microstructural characteristic properties of the real domain and various subdomains (1/4th, 1/9th, and 1/16th of the real domain volume) for the Ni-GDC anode. The table shows that the volume percentages of Ni, GDC, and pore phases exhibit minimal variation across all subdomains, indicating that the chosen subdomains adequately represent the bulk properties. Specific surface areas for Ni-Pore and GDC-Pore show relatively higher deviations in the 1/16th subdomain compared to the other subdomains. In contrast, the Ni-GDC interface remains consistent across all subdomains. Tortuosity values vary with smaller subdomains, with relatively high deviations suggesting that tortuosity is a more localized property and transport paths are not uniformly homogeneous across the structure. The total TPB density also shows a significant deviation from the real domain in the 1/16th subdomain. However, the average particle diameters for Ni, GDC, and pores remain consistent across all subdomains, further validating the representativeness of these smaller volumes.

Selecting the subdomain with 1/9th of the real domain volume emerges as an optimal choice, balancing computational efficiency and accurately representing the real domain's microstructural properties. This subdomain size retains the essential characteristics of the real domain while significantly reducing computational demands compared to the larger 1/4th subdomain. Consequently, the 1/9th subdomain size is ideal for performing efficient phase-field simulations without compromising the fidelity of the microstructural representation. In contrast, the 1/16th subdomain, while further reducing computational load, may not be as suitable. The larger deviation in TPB density and the increasing tortuosity deviations indicate that the smallest subdomain may not capture the complex microstructural details as accurately as the larger subdomains. Therefore, the 1/16th subdomain could potentially lead to less reliable simulation results, making it a less optimal choice for accurate phase-field simulations.

In order to assess the effects of statistical fluctuations and verify the representativeness of the selected subdomain, we performed a quantitative error analysis based on variations in microstructural properties in nine non-overlapping subdomains, each comprising 1/9 of the total volume. For each subdomain, the microstructural properties are calculated, and their statistical variability is assessed in relation to the values of the original

Table B2. Microstructural characteristic properties of pristine and subdomains of various volumes.

Parameter	Real domain	1/4th of real domain	1/9th of real domain	1/16th of real domain
Ni Vol%	22.44	22.60	21.92	22.00
GDC Vol%	41.38	40.73	41.57	42.06
Pore Vol%	36.18	36.67	36.51	35.94
Ni/Pore Specific Area (μm^{-1})	0.37	0.37	0.36	0.34
GDC/Pore Specific Area (μm^{-1})	1.50	1.49	1.51	1.52
Ni/GDC Specific Area (μm^{-1})	0.67	0.67	0.67	0.67
GDC Tortuosity (–)	2.57	2.56	2.51	2.46
Pore Tortuosity (–)	2.57	2.57	2.68	2.74
Total TPB density (μm^{-2})	1.82	1.81	1.80	1.73
Nickel Avg. Particle Diameter (μm)	0.91	0.92	0.93	0.93
GDC Avg. Particle Diameter (μm)	0.59	0.58	0.58	0.58
Pore Avg. Particle Diameter (μm)	0.60	0.62	0.62	0.61
Total volume (μm^3)	6666	1664	743	417
Voxel size (μm)	0.05	0.05	0.05	0.05

domain. The results, summarized in **Table B3** and illustrated in **Figure B1a** in B, show that the coefficient of variation (CV) for all nine microstructural properties is in the range of 1 to 5%, with a mean CV of about 3%, indicating low variability. Furthermore, based on the law of large numbers and assuming statistical independence of the subdomains, the statistical uncertainty of the properties of the total volume is only approximately $\sqrt{1/9} = 1/3$ of the observed scatter of the subdomains. Thus, the expected CV for the total volume for all properties is less than 2%. In comparison, the aged microstructure exhibits property changes of up to 20% compared to the pristine state, with a mean deviation of about 11%. Although the pristine and aged microstructures were reconstructed from distinct regions, both originate from relatively central areas of the anode, minimizing edge effects and spatial heterogeneity. This is supported by a statistical analysis of four non-overlapping 1/2 subdomains of the original microstructure, which shows CV values between 0 and 2% across all properties, indicating negligible spatial variations (see **Table B4** and Figure B1b in B). Furthermore, the volume of the original microstructure exceeds the threshold for the representative volume element (RVE) of 10^3 particles, where most properties converge to stable values, as concluded by Joos et al.[65]

2.6. Active Learning Framework

2.6.1. Virtual Research Environment

The research was conducted within Kadi4Mat,[36] our research data infrastructure that supports FAIR modeling of scientific processes. Kadi4Mat integrates modules such as a community repository and an electronic lab notebook, which facilitate data management, workflow automation, and reproducibility. A core feature of the Kadi ecosystem is its visual workflow functionality, provided through KadiStudio.[66] KadiStudio is a standalone desktop application within Kadi4Mat that functions as a workflow editor, allowing users to design and execute scientific processes visually. These workflows, composed of interconnected nodes with distinct functionalities, enable structured storage, visualization, and sharing through seamless communication with KadiWeb. Our AL framework is implemented as part of KadiAI, the Kadi4Mat's interface for Machine Learning and Artificial Intelligence, and made available as a collection of workflow nodes. The framework leverages the features of the overarching system while enhancing and expanding its functionalities. Additionally, by integrating pre-existing libraries such as TensorFlow-Keras[67] and

Table B3. Evaluation of statistical fluctuations in microstructural properties over 1/9th of real domains.

Parameter	Mean	Standard Deviation	Coefficient of Variation (%)
Total TPB density (μm^{-2})	1.79	0.074	4.13
Ni/Pore Specific Area (μm^{-1})	0.37	0.016	4.41
Ni/GDC Specific Area (μm^{-1})	0.67	0.023	3.47
GDC/Pore Specific Area (μm^{-1})	1.50	0.028	1.87
GDC Tortuosity (–)	2.60	0.138	5.29
Pore Tortuosity (–)	2.61	0.133	5.08
Nickel Avg. Particle Diameter (μm)	0.91	0.0247	2.71
GDC Avg. Particle Diameter (μm)	0.59	0.008	1.38
Pore Avg. Particle Diameter (μm)	0.60	0.014	2.33

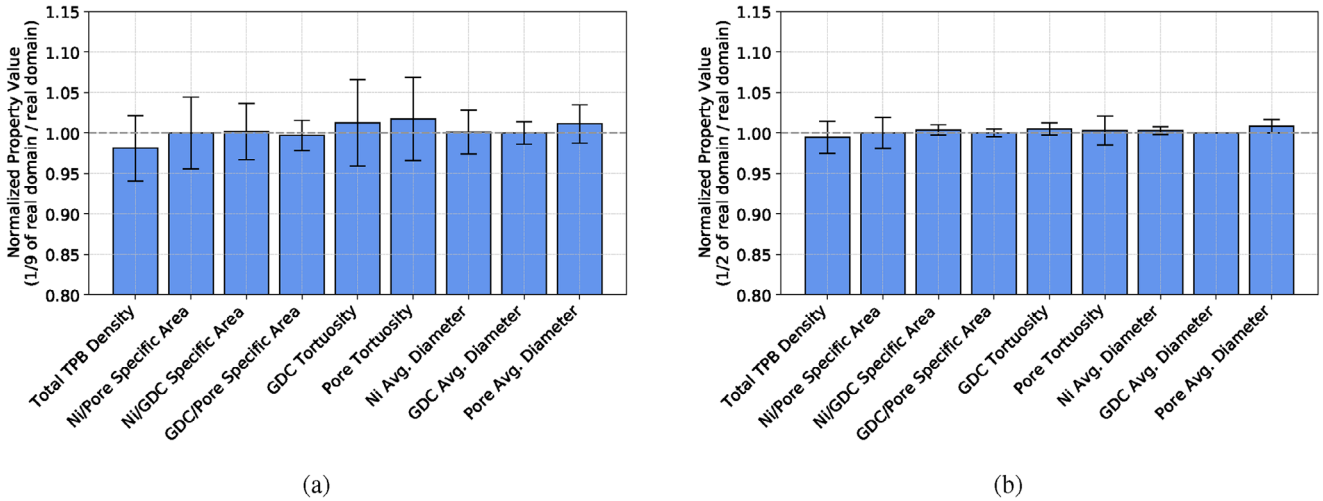

Figure B1. Comparison of normalized microstructural properties variations over different subdomain sizes against the real domain. a) Normalized property values and error bars for the nine subdomains of size 1/9. b) Normalized property values and error bars for the four subdomains of size 1/2. Each bar represents the mean value across the subdomains, with the error bars indicating the standard deviation. The values of the real domain are used as a normalization reference.

scikit-learn,[68] we ensure compatibility with widely-used standards and robust performances.

2.6.2. Bayesian Optimization

Bayesian Optimization (BO) is a sequential, surrogate-based method designed for optimizing expensive-to-evaluate black-box functions, such as those encountered in modeling the complex microstructural evolution of SOFC anodes. The methodology becomes especially valuable in our study, which involves navigating a 7-dimensional parameter space defined by feasible values for seven key input parameters used in multi-phase field simulations (namely, interfacial energies and excess interface diffusivities), whose interrelationships are intricate and often poorly characterized. The general optimization task can be formalized as:

$$\min_{x\in\mathcal{X}} f(x), \quad \mathcal{X} \subseteq \mathbb{R}^n \tag{13}$$

where f is a derivative-free, potentially non-convex, and possibly noisy function, whose evaluations are computationally expensive and therefore limited. In our case, f measures the discrepancy between simulated and experimental microstructural properties of the Ni-GDC anode; for details, see Section 3.1. BO addresses this by constructing a probabilistic surrogate model (typically a Gaussian Process) over f, which can be iteratively updated and queried to inform optimization decisions. The model, rooted in Bayes' theorem, combines the *prior* knowledge about the space of possible objective functions, with the *likelihood* of the observed data $\mathcal{D}$, generating a *posterior* distribution,

$$P(f|\mathcal{D}) \propto P(\mathcal{D}|f)P(f) \tag{14}$$

which represents our updated beliefs about the objective function f, given observed data $\mathcal{D}$. A popular technique is to treat the problem as a Gaussian process regression model. A Gaussian Process (GP) is an extension of a multivariate Gaussian distribution to a stochastic process that constructs a joint Gaussian distribution over all finite selections of function values.[69] A GP is fully

Table B4. Evaluation of statistical fluctuations in microstructural properties over 1/2 of real domains.

Parameter	Mean	Standard deviation	Coefficient of Variation (%)
Total TPB density (μm^{-2})	1.810	0.036	1.99
Ni/Pore Specific Area (μm^{-1})	0.370	0.007	1.91
Ni/GDC Specific Area (μm^{-1})	0.673	0.004	0.64
GDC/Pore Specific Area (μm^{-1})	1.50	0.007	0.47
GDC Tortuosity (–)	2.583	0.019	0.74
Pore Tortuosity (–)	2.578	0.046	1.79
Nickel Avg. Particle Diameter (μm)	0.913	0.004	0.47
GDC Avg. Particle Diameter (μm)	0.590	0.000	0.00
Pore Avg. Particle Diameter (μm)	0.605	0.005	0.83

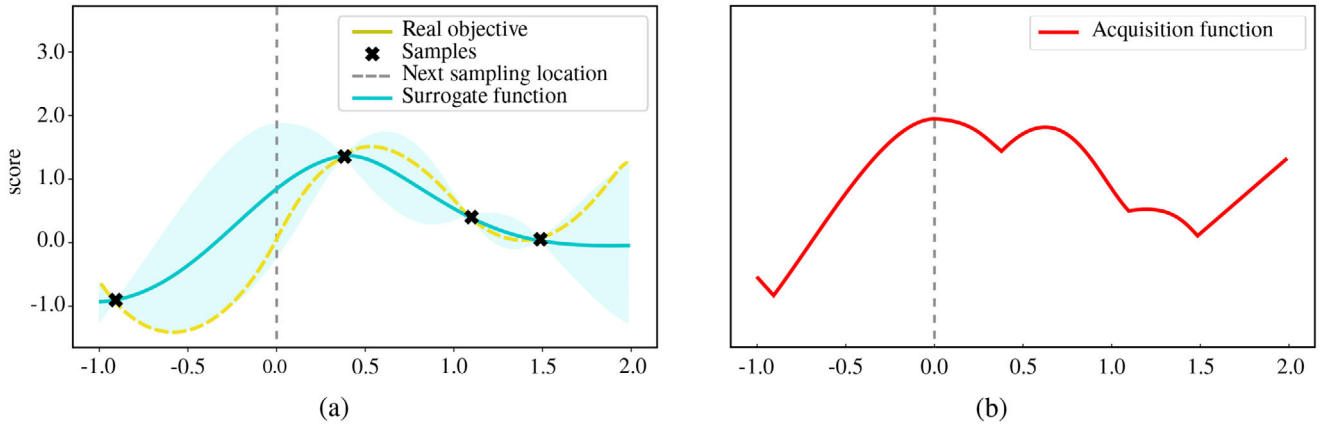

Figure 4. Representative iteration of the BO algorithm employed for a synthetic 1D BO maximization problem. The BO method quantifies the uncertainty (light blue areas) around its prediction (blue line), allowing informed decisions for selecting the next sample. At each step, the data point to be sampled is determined by maximizing the acquisition function (b), which in this case is the UCB. This visualization is automatically generated by the framework for every 1D optimization problem, and uploaded in Kadi.

specified by its mean $\mu(\mathbf{x}) = E[f(\mathbf{x})]$ and covariance (or kernel) function $k(\mathbf{x}, \mathbf{x}') = E[(f(\mathbf{x}) - \mu(\mathbf{x}))(f(\mathbf{x}') - \mu(\mathbf{x}'))]$, as:

$$f(\mathbf{x}) \sim \mathcal{GP}(\mu(\mathbf{x}), k(\mathbf{x}, \mathbf{x}')) \tag{15}$$

representing respectively the model's prediction and uncertainty in the objective function at the point $\mathbf{x}$, see **Figure** 4a. At each iteration, the method selects the next evaluation point by maximizing an acquisition function (Figure 4b) that controls the decision-making process. This function interprets the GP model's predicted mean and variance, balancing exploration of new areas with exploitation of known promising regions. After each evaluation of the objective function, the surrogate model is updated with the new data point. This iterative process refines the surrogate model's understanding of the objective function landscape, enabling increasingly accurate predictions. Compared to grid search, which becomes computationally prohibitive in our 7-dimensional parameter space by evaluating all combinations uniformly, BO significantly reduces the computational burden by targeting only the most informative regions. Similarly, in contrast to genetic algorithms, which rely on stochastic variation and lack explicit modeling, BO leverages a probabilistic surrogate to guide the search more efficiently and typically reaches comparable solutions with fewer evaluations.

2.6.3. Scientific Workflow Implementation

The AL framework used for this study is provided entirely as a modular collection of workflow nodes, each designated for a specific function (see **Figure** 5 for details). The workflow consists of five main groups of nodes that manage the complete data process: pre-processing Figure 5c, simulation and cluster communication Figure 5d, post-processing Figure 5e, and two AL components: the BO Oracle Figure 5b and the Scorer Figure 5f. The BO Oracle node encapsulates the AL-concept of an oracle, selecting data points for evaluation to progressively refine model performance. Upon execution, this node retrieves necessary information for the search from KadiWeb, specifically from an "umbrella" Record containing the optimization objective (minimization or maximization), tunable parameters, and their valid ranges. Based on the information extracted from the umbrella record, the Oracle employs BO to efficiently explore the high dimensional parameter space and suggest the next parameter configuration. Specifically for this study, we used the scikit-learn implementation and fit a GP regression model with Matérn kernel[69] with smoothness parameter $\nu = 2.5$ and lengthscale $\ell = 1.0$. Matérn-5/2 ($\nu = 2.5$) is often adopted in BO literature[70,71] for moderate-dimensional problems since it provides a good balance between smoothness and flexibility of the learned function. As an acquisition function, we used the popular upper confidence bound (UCB), due to its strong theoretical guarantees of sublinear cumulative regret, particularly when used with Matérn kernels. Furthermore, this choice provided a transparent and tunable mechanism for balancing exploration and exploitation through the explicit formulation of UCB:

$$UCB(\boldsymbol{x}, \beta) = \mu(\boldsymbol{x}) + \beta\sigma(\boldsymbol{x}) \tag{16}$$

i.e., a weighted sum of the expected value μ and the uncertainty given by the standard deviation σ of the Gaussian Process. The weight is given by β, the trade-off parameter between exploration and exploitation. When β is small, BO prioritizes areas of the parameter space with high expected performance, when instead β is high, BO incentivizes the exploration of unknown regions.

The next question to address is how the model assesses each trial to determine its relevance to the optimization objective. AL algorithms employ a scoring system to prioritize samples with the highest potential to yield valuable information and enhance the learning process. In this framework, the Scorer–our second core component–implements this scoring mechanism, defining the metric that assesses each simulation trial. This metric, or objective function, provides a quantitative measure of the outcome's alignment with the desired target. The Scorer node computes this metric for each iteration, i.e., for each simulation trial, providing feedback that directs the Oracle's navigation of the parameter space. The iterative process can be terminated once either a specified maximum number of iterations is reached, or an optimum

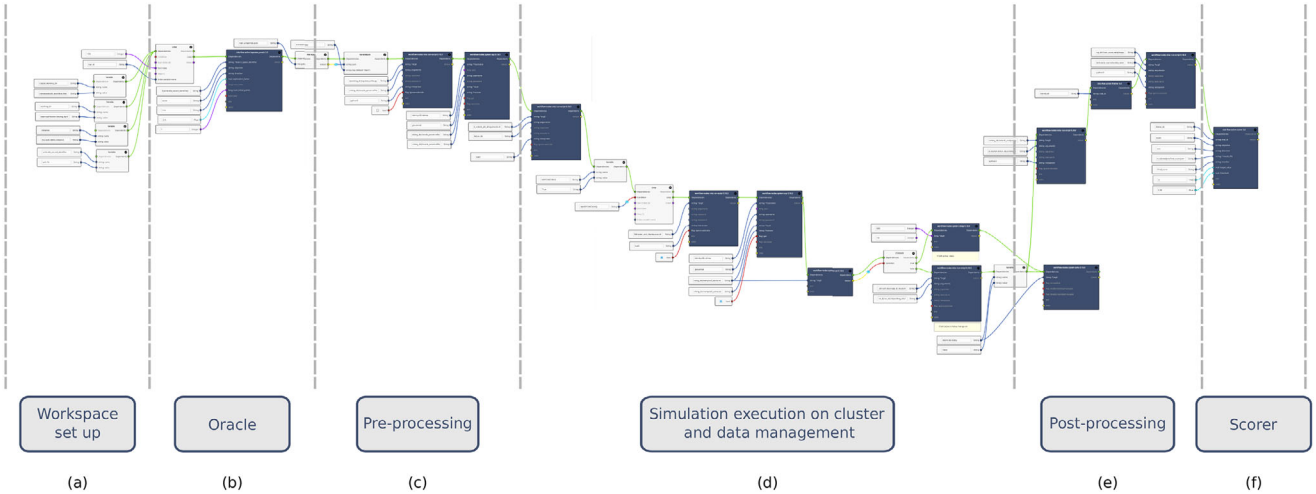

Figure 5. Visualization of the workflow created within KadiStudio to automate the parametrization study of Ni-GDC anodes in SOFCs. The workflow progresses as follows: a) user-input nodes configure environment variables, working directories, and tokens for the communication with KadiWeb, streamlining the process; b) a node enclosing the Bayesian Oracle; c) pre-processing nodes that convert the Oracle output into Pace3D simulation input data; d) nodes that submit simulation jobs to the cluster and monitor the execution; e) post-processing nodes for result analysis; and f) a scorer node that rates the simulation outcome based on the study's objective. Each node automatically updates the corresponding Records in Kadi4Mat with newly acquired information.

value is found within a user-defined threshold. In this work, we chose as the objective of the optimization a metric of the deviation between the experimental and simulated aging of the SOFC anode. For simplification, on the main part of this work, we extrapolate the nine most meaningful parameters describing the final microstructure and measure the discrepancy between the target and the obtained values. The score assigned to each trial quantifies this discrepancy. Our objective is, therefore, to minimize this distance, which frames the study as a minimization problem. A smaller distance results in a lower score, indicating a closer replication of the desired microstructure, and therefore a better performance.

2.6.4. Data Management and Knowledge Graph Representation

Each parameter configuration suggested by the Oracle automatically triggers the creation of a Record, the basic structured data entry of Kadi. The available information for each individual evaluation (or trial), including the simulation results, is contained in the Kadi Record and continuously updated through the optimization process. An additional "umbrella" Record, linked to every trial Record (see **Figure 6**), provides an overview of the entire search from the starting setting of the study (parameter ranges, objective function, type of optimization), to the best result available at every step.

Additional visualization options are available to aid in the analysis and interpretation of the optimization process. For multidimensional optimization problems, parallel coordinate plots are a good solution to have an overview of the search, visualize the parameter space exploration, and the current best results. Our framework automatically produces parallel plots at each iteration (see **Figure 7**). These plots display each trial as a polyline intersecting parallel axes, where each axis represents a parameter or the objective score, enabling efficient comparison of multiple trials and identification of trends across the parameter space. An iteration-specific (Figure 7a) and an overview parallel plot (Figure 7b) are constantly updated and automatically uploaded respectively in the trial Records and in the umbrella Record.

3. Results and Discussion

The developed AL framework was exploited to optimize a wide set of parameters for phase-field simulations of coarsening in Ni-GDC anode under specific operating conditions. In this section, we present the results of our study and discuss their implications. A proof of concept, demonstrating our method's potential for efficient parameter optimization in both single- and multi-dimensional problems, is detailed in A. Following validation, the framework was applied to 3D FIB-SEM reconstructed Ni-GDC anode microstructures. In this section, we present the results of both single- and multi-objective formulations of the considered optimization problem.

3.1. Framework on 3D FIB-SEM Reconstructed Ni-GDC Anode Microstructures

The FIB-SEM reconstructed experimental microstructures of Ni-GDC anode, both in pristine condition and after 240 hours of aging under given operating conditions, are now used as a reference in the AL framework. At this stage, the goal is to identify an optimal set of input parameters that most accurately replicate the target microstructure properties observed in the FIB-SEM experimental data.

3.1.1. Single Objective Optimization

Building on the successful validation of our approach, we apply the AL framework to address the core scientific objective of this

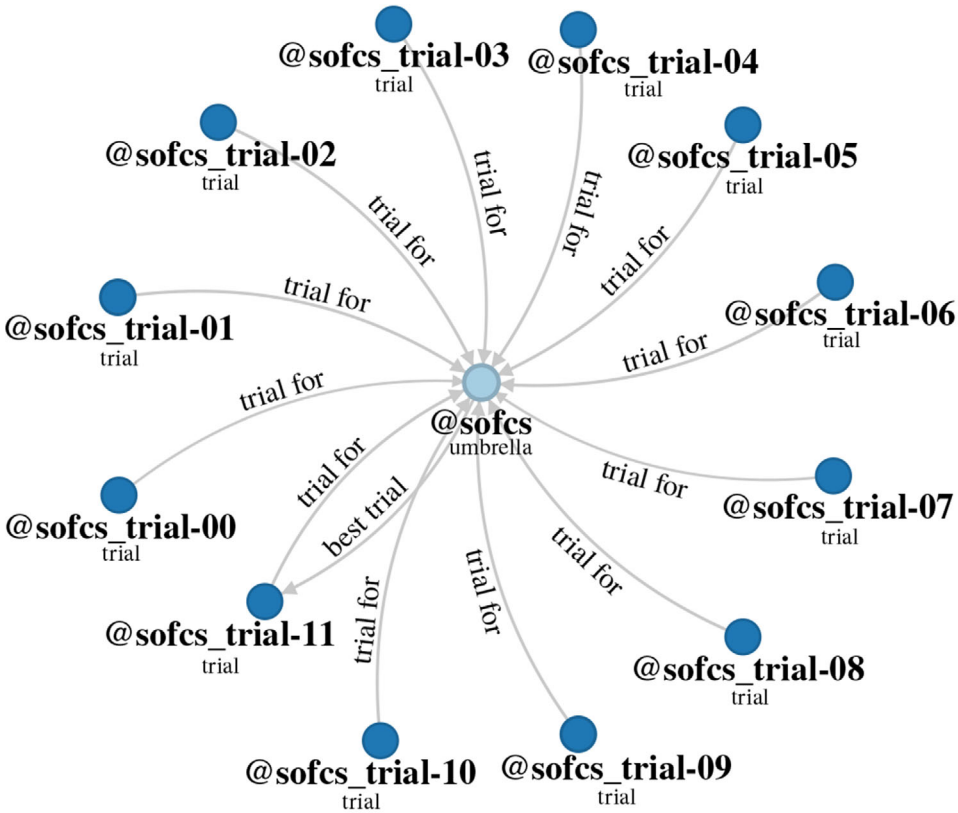

Figure 6. Visualization via Kadi4Mat of the results of our AL framework applied to the 5-dimensional SOFCs optimization problem. Every circle represents a Kadi Record, which includes all the associated information, i.e., metadata and files. The Record links in the picture clearly visualize all trial configurations and the current optimal configuration. All the trial Records (dark blue) are linked to the umbrella Record (light blue) with the label "trial for", while a second link, "best trial", denotes the optimal configuration Record.

study: identifying an optimal parameterization for a Ni-GDC anode coarsening model under given operating conditions. Thanks to the Kadi4Mat RDM environment, which integrates our entire data workflow, a seamless transition from the validation phase to the subsequent stages was straightforward.

As explained in Section 2.5, subdomains of real microstructures were employed, since repeatedly simulating the entire microstructure within the framework is computationally prohibitive. A subdomain with $9.4 \times 12.4 \times 6.4\ \mu m^3$ of volume was selected as the initial structure for the multiphase-field simulations. Given the inherently destructive nature of FIB-SEM techniques, the pristine and aged experimental microstructures originate from different regions within the Ni-GDC anode rather than from a consistent, singular location. This variability limits direct comparisons of aging between simulated and experimental structural morphologies. As a result, we focus our benchmark on the

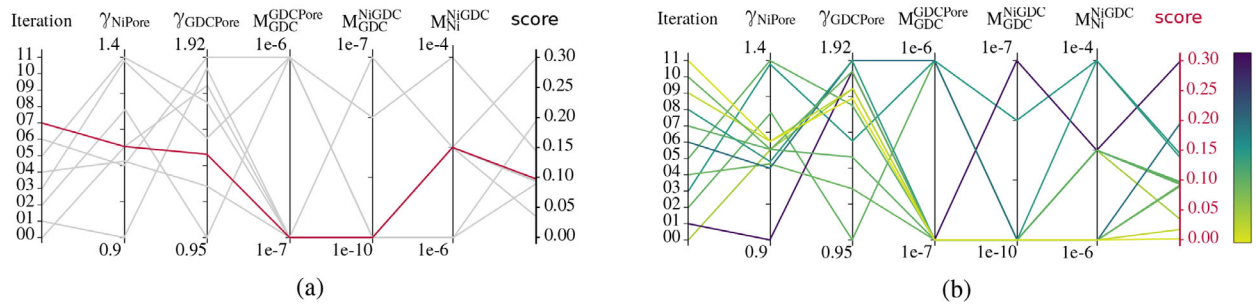

Figure 7. Example parallel coordinates plots produced by the AL framework. These plots visually represent the progression of the parameter search. Each trial Record in Kadi contains a file showing the iteration-specific result (a). The plot displays the chosen parameter values and a score rating of the results in the form of gray lines for the past iterations, and a red line for the current one (iteration 7 in the example figure). Furthermore, the umbrella Record contains an overview parallel coordinates plot (b) showing all the results of the search, each line representing one trial. The coloring of each line is based on the obtained score. This plot is automatically updated and uploaded into Kadi every time a new evaluation is made.

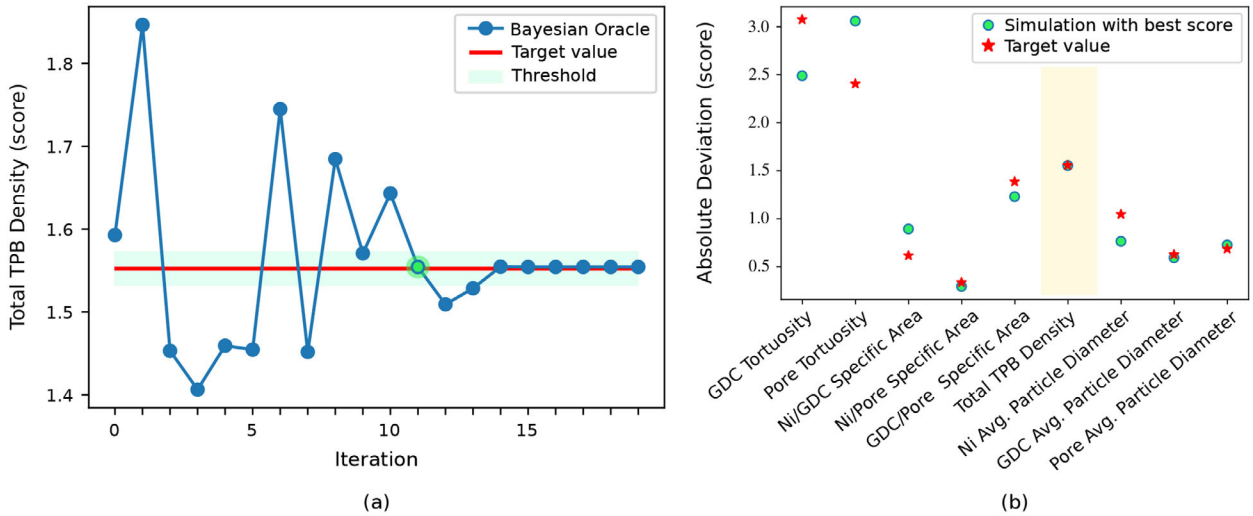

Figure 8. a) Search overview of a 5D, single objective optimization, with total TPB density used as scoring value. Target value for total TPB density found at iteration 11. b) A comparison is presented between the target values for nine considered microstructure properties and those obtained from the Oracle-guided simulation at iteration 11. The plot demonstrates that the parameter considered for scoring closely matches the target, while others mostly deviate from their respective target values.

total density of the TPB, an important microstructural parameter that reflects the phenomena of the aging process. This approach provides a more reliable benchmark for comparing the aging of simulated and experimental microstructures, circumventing the limitations of localized structural variations.

As design variables for our AL Bayesian study, we considered the parameters γ_{NiGDC}, $\gamma_{GDCPore}$, $M_{\mathrm{GDC}}^{GDCPore}$, M_{GDC}^{NiGDC}, M_{Ni}^{NiGDC}, resulting in a 5D search space. For each of these parameters, we defined a range of plausible values based on available literature data and physical constraints (see Table 1). Although the values for nickel's surface energy and surface diffusion coefficient show considerable variation across different sources, they remain well-documented in the literature and are better established than those for GDC. For this study, we used fixed values of 2.26 J/m^2 for the surface energy[18] and 5.48×10^{-22} m^3 s^{-1} for the surface diffusion coefficient, toward lower end of the value range and approximately one-third of minimum value from Blakely et al.[41] under the given operating temperature of 900°C. Using these fixed values across all simulations reduces the dimensionality of the search space, ensures a consistent scaling system of the model, and simplifies the calculation of other parameters.

The framework structure established during the validation stage (see A), along with the KadiStudio workflow automating the whole process (Figure 5), remains fundamentally unchanged, aside from a few adjustments. Due to the significant increase in computational resources required by the simulations, we have included in our data stream a component that handles the automated communication with an HPC cluster. Each simulation was run on the idm-hpc03 high performance computing cluster, which consists of eight computing nodes, each equipped with 64 cores. This cluster is part of the network infrastructure of the Institute of Digital Materials Science (IDM), and all computational tasks were managed using the SLURM workload manager. For the purposes of this study, five nodes of the cluster were employed to perform the computations. At each iteration of the framework, the Bayesian Oracle provides its prediction of the most informative data point in the form of a complete parameters' configuration. The oracle's output is subsequently input into a job file designed to initiate Pace3D simulations with the specified values. The job is then submitted to a computing cluster using SLURM and constantly monitored until completion, at which point the results are retrieved for post-processing and scoring. The framework was furthermore modified to incorporate a new scoring metric based on the total triple-phase boundary (TPB) density, a primary parameter characterizing the resulting microstructure. This new metric quantifies the deviation of the simulated TPB density from the experimentally measured value of the target microstructure. In other words, the objective of the Bayesian Oracle at this phase is to mimic the total TPB density of the target microstructure, assessing whether this replication suffices for a comprehensive comparison of the entire microstructure. **Figure** 8a shows an overview of the 5D optimization search, finding the target value of 1.55 at iteration 11, and definitively converging at iteration 14. The model successfully minimized the deviation for the single objective parameter, demonstrating its capability in a focused optimization scenario. However, analyzing Figure 8(b), we can conclude that a perfect match of a single considered property or descriptive parameter is insufficient to fully capture the morphology of the entire Ni-GDC anode microstructure, as significant deviations are observed when evaluating other critical descriptive parameters. To address this limitation, it is essential to adopt a more comprehensive approach, ensuring that all key characteristics are effectively considered and represented in the optimization process.

3.1.2. Multi-Objective Optimization: Weighted sum Scalarization Approach

As demonstrated in the previous section, it is crucial to consider multiple aspects of the microstructure of Ni-GDC anodes to

achieve a comprehensive representation that can effectively guide the optimization process. Ideally, we aim to closely replicate the nine most critical microstructure properties of the reference microstructure: GDC Tortuosity, Pore Tortuosity, Ni-GDC Specific Area, Ni/Pore Specific Area, GDC/Pore Specific Area, Total TPB density, Nickel Avg. Particle Diameter, GDC Avg. Particle Diameter, Pore Avg. Particle Diameter (for more details, refer to Section 2.4 and Table B1).

Multi-objective optimization techniques facilitate the simultaneous optimization of multiple criteria by considering different objective functions. The goal for these problems is to find a set of solutions that represent the best trade-offs among the objectives. This set of solutions is known as the Pareto optimal set or Pareto front when referring to the image of the Pareto Set in the objective space (refs. [72] and [73]). Each solution in this set is non-dominated, meaning that it's not possible to improve one objective without worsening at least one other. Building on this concept, for the final improved configuration of our AL framework, we define an objective function for each of the mentioned key properties, thereby integrating all of them into the optimization process. As we are working with subdomains of the entire microstructure, in our view, aiming for equal precision in replicating all the properties is not an effective approach. Therefore, as a score metric, we employ a weighted sum scalarization approach (see e.g., refs. [74] and [75]), a method widely used to convert a multi-objective problem into a single-objective. This is achieved by forming an aggregate objective function using a linear combination of all objective functions, i.e., solving a problem of the form:

$$\min_x F(x) = w_1 f_1(x) + w_2 f_2(x) + \ldots w_n f_n(x) \tag{17}$$

where f_i are the different objective functions, and w_i the respectively assigned weights, typically normalized according to $0 \leq w_i \leq 1, \sum w_i = 1$, which leaves the parameter space with $n-1$ degrees of freedom. Adjusting the weights results in different trade-offs between the objectives, thereby emphasizing certain properties over others and leading to different optimal solutions. The strength of the weighted sum scalarization method lies in its flexibility and conceptual transparency, which allows seamless incorporation of user or domain preferences. We exploited this property to reflect tortuosity's high sensitivity to local microstructural variations (as outlined in Section 2.5). Specifically, tortuosity parameters were assigned lower weights (half those of the other five parameters). The primary purpose of the AL Bayesian framework is to efficiently explore the physical parameters space. This approach is particularly valuable for incorporating parameters with incomplete or inconsistent literature data, as well as those influenced by varying operating conditions (refer to Section 2.3 for the details). Hence, we extend the set of design variables in order to provide the Oracle with greater flexibility in exploring a now 7D parameter space. In addition to the five key input parameters discussed in the previous section Section 3.1.1, this comprehensive approach involves tuning the model parameters related to nickel's surface diffusion coefficient M_{Ni}^{NiPore} and surface energy γ_{NiPore}. The specifically selected ranges of validity are outlined in Table 1. These include three interfacial energies and four excess interface diffusivities. The interfacial energies ranges are as follows: γ_{NiGDC} from 3.0 to 1.0 J m^{-2}, $\gamma_{GDCPore}$ from 2.0 to 0.7 J m^{-2}, and γ_{NiPore} from 2.5 to 1.5 J m^{-2}. The excess interface diffusivities are considered within the following ranges: $D_{\mathrm{GDC,ex}}^{GDCPore}$ from 2.4×10^{-25} to 2.4×10^{-28} m^3 s^{-1}, $D_{\mathrm{GDC,ex}}^{NiGDC}$ from 2.4×10^{-27} to 2.4×10^{-33} m^3 s^{-1}, $D_{\mathrm{Ni,ex}}^{NiGDC}$ from 4.0×10^{-22} to 4.0×10^{-27} m^3 s^{-1}, and $D_{\mathrm{Ni,ex}}^{NiPore}$ from 4.0×10^{-22} to 4.0×10^{-20} m^3 s^{-1}. The chosen upper bounds of these parameter ranges are used to establish the model's time and energy scales across all simulation runs. Given that nickel's surface diffusion coefficient can vary by up to two orders of magnitude, it is crucial to adjust the related model parameters accordingly, such as stable time step, interface mobilities, and total simulation time. This ensures efficient usage of computational resources while maintaining a consistent representation of the physical aging of microstructures. To achieve this, the above-mentioned model parameters are fine-tuned for each simulation run based on the specific surface diffusion values for nickel selected by the Bayesian Oracle (for more details, refer to Section 2.3).

The increased dimensionality of the parameter space offers the potential for better exploration but at the price of higher computational and time demand. An explicit time integration method is used in our phase-field model, resulting in limitations on the permissible stable time step. As a result, when simulating the same physical aging time with higher values of nickel's surface diffusion coefficients, the stable time step is further limited. This results in a longer simulation time and a longer utilization of computing resources. Therefore, higher values of the surface diffusion coefficients of nickel substantially increase the computational resource requirements. As the Bayesian Oracle now navigates a more complex and challenging landscape, it is expected to require additional initial information and an overall greater number of iterations to reach optimal solutions. This translates into a preset higher number of initial random points (seven), and results in an extended timeframe to achieve satisfactory accuracy. **Figure 9** provides an overview of the framework executed with the aforementioned setting. The entire execution of 43 iterations using the Bayesian AL framework took approximately 7 days and 18 hours on the idm-hpc03 high-performance computing cluster employing 315 cores.

Since in multi-objective optimization the goal is typically to find a set of solutions rather than a single optimum data point, we consider the five best results with an overall 7–8% error, obtained at iterations 19, 27, 31, 37, and 38. **Table 2** details the values suggested by the Oracle for each one of these iterations, along with the associated errors for each microstructure parameter. The five iterations yield a total score between 0.07 and 0.08, requiring a closer analysis of the physical parameters associated with each result. The excess surface diffusivity of nickel was consistently found to be 4.0×10^{-22} m^{3}s^{-1} across all five iterations with the best scores. The value estimated from the Bayesian AL framework, 4.0×10^{-22} m^{3}s^{-1}, is approximately four times lower than the 1.74×10^{-21} m^{3}s^{-1} calculated for the {100} surface at 900 °C using the Arrhenius relation from the experimental data of Blakely et al.[41] Nevertheless, considering experimental measurement uncertainties ranging from one to two orders of magnitude, the estimated value is reasonable and aligns well with Hoffrogge et al.'s[17] assumption that diffusion along the slow {100} surface orientation is the rate-limiting factor. Furthermore, several factors need to be considered to account for the observed

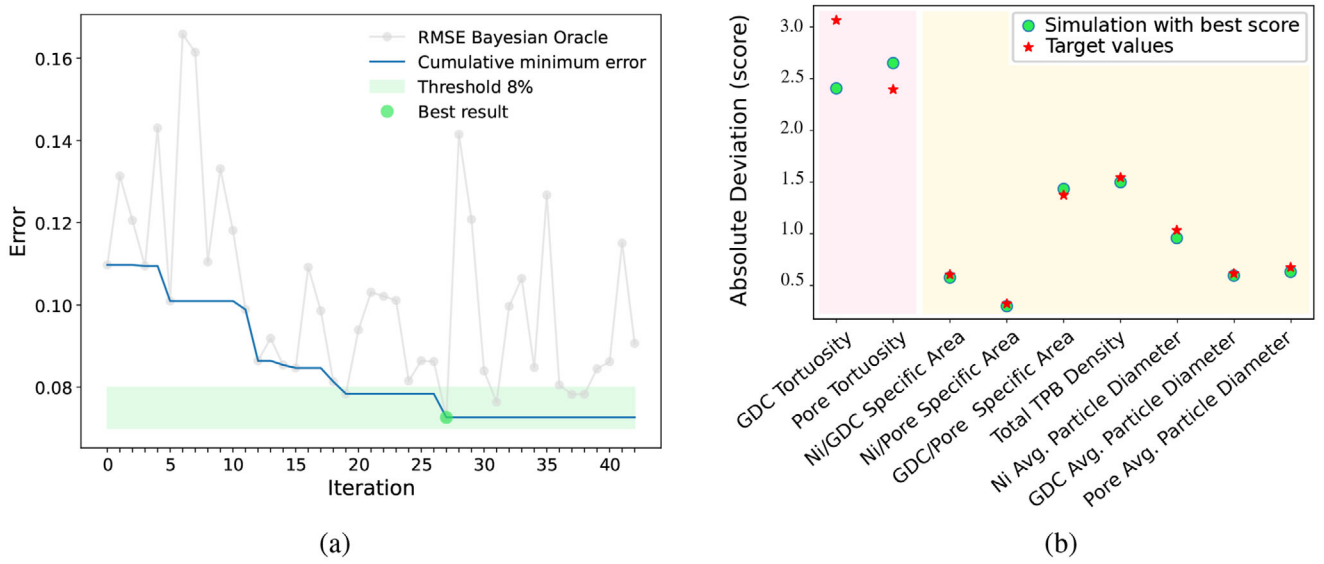

Figure 9. Convergence and parameter-match performance of the Bayesian AL framework with weighted sum scalarization approach applied to the 7D, multi-objective optimization problem as described in Section 3.1.2. a) Optimization convergence over time: The blue line shows the cumulative minimum error at each iteration, reflecting continual improvement in solution quality and evidence of plateauing around iteration 27. The grey line displays the RMSE for each iteration, providing insight into the overall search dynamics. Five iterations within the highlighted threshold achieved satisfactory accuracy ($\leq 8\%$ error). b) Agreement with target microstructural properties: Comparison of nine key descriptors–highlighting the Oracle-guided simulation at iteration 27, which delivered the best fit at 7% total error. The two tortuosity metrics (left) were assigned a lower weight during scalarization due to their higher sensitivity to local microstructural changes, while the remaining seven parameters (right) received higher weights to guide the optimization.

discrepancy: variations in experimental conditions and material purity, assumptions of isotropy, homogeneity, as well as coarsening as the primary degradation mechanism in the model, and the inherent limitations of the Bayesian multi-objective optimization framework using the scalarization approach. Nickel diffusion coefficients reported by Blakely were measured on pure nickel surfaces under high vacuum conditions ($\sim 10^{-5}$ mm Hg), whereas the present study involves a Ni-GDC composite anode operating in an atmosphere of 50% H_2 / 50% H_2O. Blakely et al.[41] reported that impurities tend to adsorb preferentially on specific crystallographic planes, particularly the (100) planes, thereby obstructing diffusion pathways and significantly reducing surface diffusion

Table 2. Overview of the 5 iterations with the best score. The top part of the table shows the values suggested by the Bayesian Oracle for each of the 7 input parameters that we asked to tune (for ranges of validity, refer to Table 1. The bottom part of the table shows the error obtained for each of the 9 considered microstructure properties in relation to the reference microstructure and the overall score.

Physical parameters	iter 19	iter 27	iter 31	iter 37	iter 38
γ_{NiGDC} (J m^{-2})	2.98	1.70	1.78	2.68	2.43
$\gamma_{GDCPore}$ (J m^{-2})	1.53	0.70	0.70	1.28	1.43
γ_{NiPore} (J m^{-2})	2.50	1.50	1.85	2.50	2.10
$D^{GDCPore}_{GDC,ex}$ (m^3 s^{-1})	2.16×10^{-26}	1.72×10^{-26}	2.07×10^{-26}	2.16×10^{-27}	4.96×10^{-27}
$D^{NiGDC}_{GDC,ex}$ (m^3 s^{-1})	1.14×10^{-33}	1.72×10^{-31}	1.14×10^{-33}	1.14×10^{-33}	1.14×10^{-33}
$D^{NiGDC}_{Ni,ex}$ (m^3 s^{-1})	4.0×10^{-27}	1.15×10^{-24}	5.40×10^{-26}	1.91×10^{-25}	4.0×10^{-27}
$D^{NiPore}_{Ni,ex}$ (m^3 s^{-1})	4.0×10^{-22}	4.0×10^{-22}	4.0×10^{-22}	4.0×10^{-22}	4.0×10^{-22}
GDC Tortuosity err	3.2e-3	2.8e-3	2.9e-3	2.4e-3	2.7e-3
Pore Tortuosity err	9.8e-4	7.5e-4	8.7e-4	5.4e-4	9.6e-4
Ni-GDC Specific Area err	7.9e-5	1.4e-4	6.0e-6	2.1e-5	4.2e-5
Ni/Pore Specific Area err	7.5e-4	2.9e-4	7.4e-4	1.0e-3	9.6e-4
GDC/Pore Specific Area err	3.3e-5	2.9e-4	1.6e-4	8.1e-4	2.3e-4
Total TPB Density err	5.2e-4	7.3e-5	2.6e-4	1.2e-4	1.8e-4
Ni Avg. Particle Diameter err	6.0e-4	5.4e-4	6.8e-4	6.2e-4	8.0e-4
GDC Avg. Particle Diameter. err	1.5e-7	4.4e-5	3.8e-5	1.3e-4	7.8e-5
Pore Avg. Particle Diameter. err	2.5e-5	3.3e-4	1.6e-4	3.9e-4	1.8e-4
final score	0.078	0.073	0.076	0.078	0.078

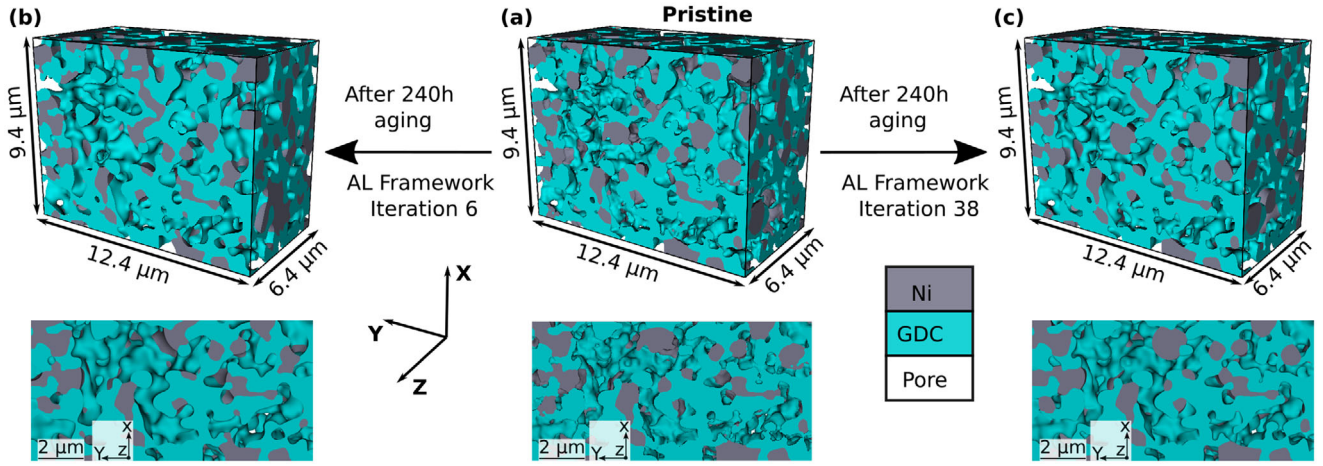

Figure 10. The figure shows the evolution of the 3D microstructure and its 2D cross-section at distinct iterations of the AL framework. a) Initial 3D microstructure for simulation and a 2D cross-sectional view of it, b) 240 h evolved 3D microstructure and 2D cross-section obtained from the AL framework at iteration 6 with a poor overall error percentage of 16.6, and c) 240 h evolved 3D microstructure and 2D cross-section obtained from the AL framework at iteration 38 with a best overall error percentage of 7.8.

rates. As a result, surface diffusion is highly sensitive to the annealing atmosphere, as adsorbed species can significantly affect atomic mobility. The operating conditions of SOFCs can influence Ni diffusivity at the surface due to oxygen partial pressure, impurities, adsorption of gas species, and interface interactions with GDC. Jiao et al.[76] reported that the wettability of Ni on YSZ improves during SOFC operation. This behavior is attributed to the adsorption of oxygen species on the Ni surface. Considering the above factors, it can be expected that the surface diffusion coefficient for Ni in the SOFC Ni-GDC system to be lower than the value reported by Blakely et al.[41] Scalarization reduces multiple objectives to a single scalar objective, potentially oversimplifying the problem and failing to capture the full range of trade-offs between competing objectives. This simplification can lead to suboptimal solutions or an incomplete representation of variability in the diffusivity estimates.

The excess surface diffusivity of GDC was found to be in the range of 10^{-26} to 10^{-27} m^3s^{-1} across all five iterations. Notably, the values from iteration 37 and iteration 38, 2.16×10^{-27} m^3s^{-1} and 4.96×10^{-27} m^3s^{-1}, closely match the literature value for the surface diffusion coefficient at 900 °C, estimated as 2.4×10^{-27} m^3s^{-1}.[55] The excess interface diffusivity of nickel along the Ni-GDC interface was 3 to 5 orders of magnitude lower than that of excess surface diffusivity. Although no direct literature is available for validation, this aligns with the general understanding that interface or grain boundary diffusion is typically lower than surface diffusion. A similar trend is observed in the excess interface diffusivity of GDC along the Ni-GDC interface.

While the absolute values of surface and interfacial energies appear to vary across the five best iterations, their ratios–a key factor in driving the system toward thermodynamic equilibrium–show a clear consistency. The values for the surface energy of nickel at iterations 19 and 37, obtained as 2.50 J/m^2, appear to disagree with values commonly reported in the literature.[18,42,45–50] Similarly, a value of 1.50 J/m^2 from iteration 27 is significantly lower than most literature findings. However, the surface energies of 1.85 and 2.10 J/m^2, obtained in iterations 31 and 38, are more in line with the reported data. For GDC, surface energies of 1.28, 1.43, and 1.53 J/m^2 in iterations 37, 38, and 19 respectively, are consistent with experimental studies using the multiphase equilibration technique, which estimate the surface energy of CeO_2 in an argon atmosphere at 900 °C to be approximately 1.80 J/m^2.[55]

Considering all physical parameters and their comparison with the available literature, the values derived from iteration 38 are proved to be consistent and representative values for aging simulations of Ni-GDC anode at given operating conditions. **Figure 10** shows the evolution of the initial 3D microstructure and its 2D cross-sectional view through distinct iterations of the AL framework. Iteration 6 produces a microstructure with an overall 16.6% error in microstructural parameters compared to experimental results, while iteration 38 reduces this error to 7.8%. The morphological differences between the aged microstructures from these two iterations are also evident in Figure 10.

4. Conclusion

Ensuring long-term reliability and sustainable operation of SOFCs requires a comprehensive understanding of the degradation processes affecting their components. Ni-GDC anode is one of these critical components undergoing significant microstructural changes over time, which impact the cell's performance and longevity. To accurately simulate the aging of Ni-GDC anodes and predict their long-term behavior under operational conditions, precise parameterization of the phase-field model is essential. However, this task is made challenging by incomplete or inconsistent literature data, especially regarding key parameters like surface diffusivities and interface energies. To address this, we presented an AL framework combined with Bayesian optimization, designed to efficiently explore the high-dimensional parameter space and identify the optimal model parameters for simulating the aging of Ni-GDC anodes.

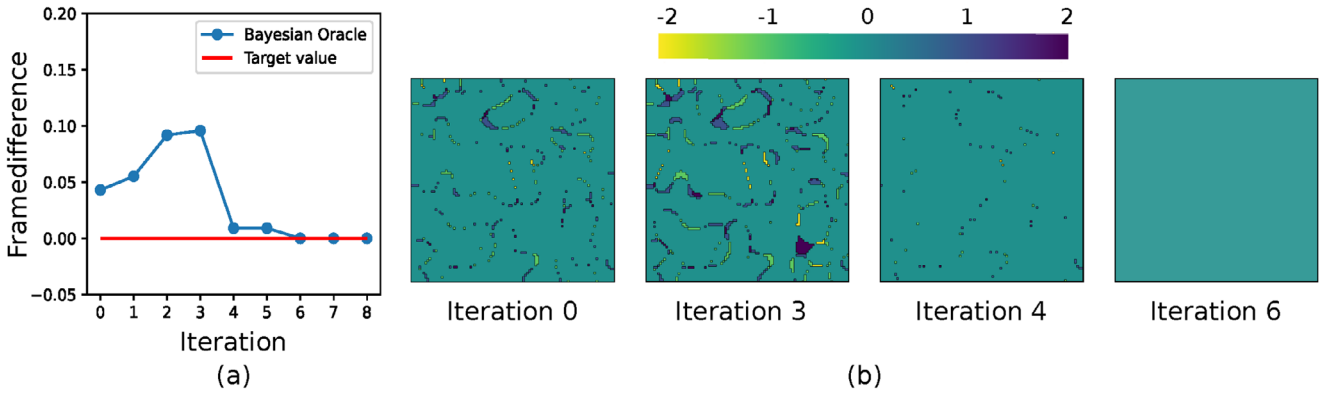

Figure A1. AL framework validation for a 1D, single-objective optimization problem. Tuned parameter: γ_{NiGDC}. The error is measured as a voxel-by-voxel difference between the resulting and target microstructure (framedifference). The first 3 data points are randomly sampled to produce a sufficient baseline for the BO Oracle search.

While single-objective optimization can simplify the design process and might be sufficiently effective in enhancing a particular material property, in the context of SOFCs Ni-GDC anodes, it does not adequately capture the full range of physical characteristics of the microstructure of interest. This approach can lead to significant deviations in other critical, descriptive parameters that are not considered, resulting in possibly sub-optimal material performances. Given these limitations, we transitioned to a multi-objective optimization approach to better address the complexity of our problem. This shift allows for the simultaneous consideration of multiple critical microstructure properties, ensuring overall improved solutions. By employing a scalarization approach, precisely a weighted sum method, we can aggregate different objective functions into a single objective, thereby balancing competing criteria and achieving a more comprehensive representation of the desired microstructure. In the context of SOFCs, we identified a promising set of solutions with an overall error on the order of 10^{-2} (specifically, between 0.07 and 0.08), indicating a good balance between competing objectives. Moreover, within this set, we identified results that align with the limited literature data available, further validating our approach. The optimized input physical parameter values obtained from our AL Bayesian framework in iteration 38 yield interfacial energies for γ_{NiGDC}, $\gamma_{GDCPore}$, and γ_{NiPore} as 2.43, 1.43, and 2.10 $\mathrm{J/m^2}$, respectively. These values align well with the available literature on the surface energies of nickel and ceria, as discussed in Section 2.3. The excess surface and interface diffusivities of nickel and GDC are $D^{NiPore}_{\mathrm{Ni,ex}}$, $D^{NiGDC}_{\mathrm{Ni,ex}}$, $D^{GDCPore}_{\mathrm{GDC,ex}}$, and $D^{NiGDC}_{\mathrm{GDC,ex}}$, with values of 4.0×10^{-22}, 4.0×10^{-27}, 4.96×10^{-27}, and 1.14×10^{-33} $\mathrm{m^3\ s^{-1}}$, respectively, under the operating conditions of Ni-GDC at a temperature of 900°C with a gas composition of H_2-50% / H_2O-50%. In conclusion, the AL Bayesian framework has demonstrated strong performances, providing good practice for intelligent data selection and model optimization. Beyond its success in finding physical parameters for Ni-GDC anode microstructure under given operating conditions, our framework's generic implementation ensures its applicability across various other applications. This approach proves particularly valuable in scenarios where missing parameters need to be inferred, or manual trial-and-error tuning is challenging, extending its utility well beyond the specific context of this study. Although this work focuses on the Ni-GDC anode system, the framework can be readily transferable to other SOFC material systems, such as the widely used Ni-YSZ anodes. For this, FIB-SEM-reconstructed experimental microstructures of Ni-YSZ in both pristine and aged states, together with appropriate adaptation of material-specific parameter ranges, such as interface energies and diffusion coefficients, are required for optimization.

The employed multi-objective scalarization approach maintains linearity, allows leveraging most of the available optimization libraries, and is generally a powerful tool when dealing with convex sets of solutions. However, for many optimization problems, the shape of the attainable set is unknown and might present non-convex regions. In these situations, a scalarization approach might fail to identify the true Pareto front, which delineates the boundary of attainable solutions, for which it is impossible to enhance any objective without adversely affecting at least one other. Even when adjusting the weights, the method can lead to unevenly distributed sets of non-dominated points in the objective function space, potentially missing critical solutions. Furthermore, while reformulating a problem with

Table A1. Overview of the values chosen by the Bayesian Oracle at iteration 22, which gave the best result. The oracle explored the parameter space within predefined constraints, alongside the specified ranges of validity. For the interface energy parameters (γ_{NiGDC}, $\gamma_{GDCPore}$), values were sampled as floats with 0.01 increment. For the diffusion coefficients related parameters (M^{NiPore}_{Ni}, M^{NiGDC}_{Ni}, $M^{GDCPore}_{\mathrm{GDC}}$, M^{NiGDC}_{GDC}), where only changes in the order of magnitude have significant impact on the outcome, the oracle selected integer values for the exponent, effectively adjusting the parameters by powers of ten. The comprehensive error, used as score for the oracle, was computed with *framedifference* according to Equation A1 and gave a result of 0.0097.

Model parameters	Given range	Reference value	Predicted value
γ_{NiGDC}	0.45 – 1.49	1.20	1.19
$\gamma_{GDCPore}$	0.29 – 0.57	0.4	0.32
M^{NiPore}_{Ni}	0.1 – 1.0	0.6	0.54
M^{NiGDC}_{Ni}	$3.52 \cdot 10^{-5} - 3.52 \cdot 10^{-2}$	10^{-3}	10^{-5}
$M^{GDCPore}_{\mathrm{GDC}}$	$3.52 \cdot 10^{-9} - 3.52 \cdot 10^{-4}$	$3.52 \cdot 10^{-6}$	$3.52 \cdot 10^{-7}$
M^{NiGDC}_{GDC}	$3.52 \cdot 10^{-11} - 3.52 \cdot 10^{-5}$	$3.52 \cdot 10^{-7}$	$3.52 \cdot 10^{-4}$

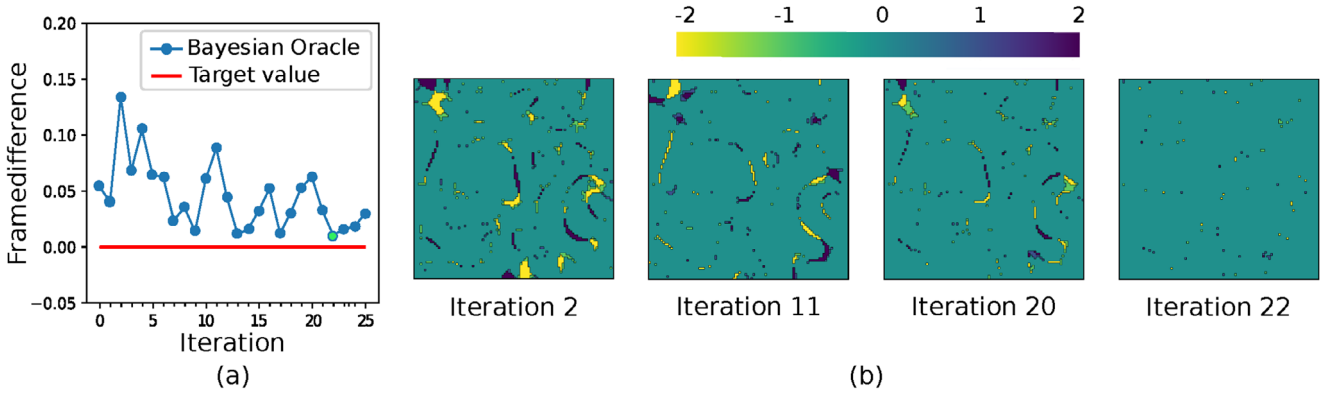

Figure A2. Framework validation for a 6D, single-objective optimization problem. The figure shows the overview of the search (a) and a visualization of the error at four different iteration steps (b). The error is measured as a voxel-by-voxel difference of the resulting and target microstructure (framedifference). The best result is found at iteration 22, with a framedifference error of 0.0097.

non-competing objectives into a single-objective framework is beneficial, other methods can produce better results for a problem with competing objectives, especially when aiming to optimize material properties. To better address the case of interdependent or inversely related material properties, further research will focus on the integration of different multi-objective approaches (like evolutionary algorithms)[77,78] within the presented framework.

Appendix A: Framework Validation

The initial AL framework validation study demonstrates the reliability and effectiveness of our method. For the validation run, we conduct a single-parameter optimization, focusing on the interfacial energy between nickel and GDC γ_{NiGDC}, while keeping the other parameters fixed. A 2D reference structure is generated by initially creating a Voronoi structure consisting of nickel, GDC, and pore phases, and then by applying phase coarsening through phase-field simulations. Interface energy between nickel and GDC (γ_{NiGDC}) of 0.577 (in model scale units) is used in model parameters. All parameters are expressed in model scale, as the focus of this validation is on testing the framework against provided model parameters rather than directly correlating with aged experimental microstructures or physical properties. The AL framework is then employed to tune the parameter γ_{NiGDC} within a physically meaningful range (0.4 – 1.2). The Oracle initiates the Bayesian search by performing three iterations of random search, providing initial seeds to construct the probabilistic model of the objective function. Each parameter value selected by the Oracle for γ_{NiGDC} is automatically passed to the phase-field simulations, executed with the in-house developed framework Pace3D (Parallel Algorithms for Crystal Evolution in 3D).[79] Upon completion, simulation results are evaluated and scored, providing valuable information for strategic navigation of the search space. Throughout our study, the score represents a quantitative measure of deviation from the target microstructure. In Pace3D, the microstructure is stored in a 2D/3D grid, with each voxel assigned to one of the phases ϕ_{Ni}, ϕ_{GDC} and ϕ_{Pore}. For the validation phase of the study, we chose a voxel-wise frame-difference score, calculated as follows:

$$\text{score} = \sum_{\nu=1}^{N} |\phi_i^{\text{sim}}(\nu) - \phi_i^{\text{reference}}(\nu)|, \qquad i \in \{\text{Ni, GDC, Pore}\} \tag{A1}$$

where ν represents each voxel of the grid, and N the total number of voxels. These computations are enclosed within a Pace3D post-processing tool called *framedifference*, which facilitates streamlined assessment of microstructure deviations.

Minimizing the deviation is a successful validation step, which leads to the identification of the correct model parameters. Our AL framework converged at iteration 6 (see **Figure A1**), yielding results that closely aligned with the target parameters and successfully validated the 1D problem. The best value found for the parameter γ_{NiGDC} was 0.57715, with a target value of 0.57700 and an accepted threshold of 0.02.

To address the complexity of the SOFC's microstructural evolutions, we moved to a more advanced multidimensional validation phase, optimizing six parameters simultaneously. The chosen parameters (discussed in detail in Section 2.3), together with their ranges of validity, and the best results obtained after 25 iterations of our framework, can be seen in **Table A1**. For this second validation phase, the scoring mechanism remained unchanged, i.e. as in Equation A1, for each iteration of the method, we measured the deviation of the resulting microstructures from the reference. A shorter simulation time was considered to save computational resources and time, as the purpose here was still pure validation, giving no meaningful scientific results. Consequently, while the results obtained by the framework for some parameters may not appear optimal at first, there are a few factors to take into consideration. The terms in the model that are related to the interface energy and nickels surface diffusion coefficient (first three in Table A1), have a greater influence on the microstructure at smaller time frames, while the other terms in the model related to diffusion coefficients (last three in Table A1), only cause notable changes in the microstructure over an extended simulation period, due to their low magnitude of values. It is therefore logical for the firsts, to approximately reach the reference value, while for the lasts, a closer alignment with the reference value is expected in longer simulation times. It is important to note that the diffusion values were restricted to variations by orders of magnitude, leading to the reference and predicted values aligning precisely with the same coefficient values. Furthermore, as the dimensionality of the problem increases, the volume of the search space expands exponentially, and so does the number of evaluations needed to ensure thorough exploration. **Figure A2** shows an overview of the search.

Acknowledgements

Most of this work was computed on the idm-hpc03, HPC cluster of the Institute of Digital Materials Science (IDM), Karlsruhe University of Applied Sciences. The authors acknowledge the assistance of the State of Baden-Württemberg through bwHPC. The authors gratefully acknowledge funding from the Federal Ministry of Education and Research in the framework of the WirLeben-SOFC project (BMBF, funding code 03SF0622D). Additional support is provided by the Helmholtz association, programme "Materials Science and Engineering (MSE)", no. 43.31.01, which is gratefully acknowledged. The authors would like to thank the NHR-Verein e.V. (www.nhr-verein.de) for supporting this work within

the NHR Graduate School of National High Performance Computing (NHR).

Author Contributions

R.-K.-J. and G.-T. contributed equally to this work. R.K.J. and G.T. were primarily responsible for the conceptualization of the study, along with contributions to methodology, software development, visualization, validation, and drafting the original manuscript as well as reviewing and editing it. M.A. contributed to the methodology, software, visualization, and validation aspects. M.W. supported the project through funding acquisition, provision of resources, and also participated in the study's conceptualization and drafting of the original manuscript. A.K contributed to the methodology, software development, project administration, and conceptualization, along with reviewing and editing the manuscript. B.N. played a key role in funding acquisition, project administration, and supervision, while also being involved in the conceptualization and manuscript review and editing. D. S. contributed to the methodology, project administration, and conceptualization, as well as the review and editing of the manuscript.

Conflict of Interest

The authors declare no conflict of interest.

Data Availability Statement

The data that support the findings of this study are available from the corresponding author upon reasonable request.

Keywords

active learning, Bayesian optimization, coarsening, Kadi4Mat, KadiAI, phase-field modeling, solid-oxide fuel cells

Received: March 3, 2025
Revised: June 9, 2025
Published online: July 2, 2025

[1] M. Singh, D. Zappa, E. Comini, *Int. J. Hydrogen Energy* **2021**, *46*, 27643.
[2] R. M. Ormerod, *Chem. Soc. Rev.* **2003**, *32*, 17.
[3] A. Zekri, M. Knipper, J. Parisi, T. Plaggenborg, *Phys. Chem. Chem. Phys.* **2017**, *19*, 13767.
[4] M. Trini, A. Hauch, S. De Angelis, X. Tong, P. V. Hendriksen, M. Chen, *J. Power Sources* **2020**, *450*, 227599.
[5] L. Holzer, B. Iwanschitz, T. Hocker, B. Münch, M. Prestat, D. Wiedenmann, U. Vogt, P. Holtappels, J. Sfeir, A. Mai, Th. Graule, *J. Power Sources* **2011**, *196*, 1279.
[6] Y. Liu, F. Wankmüller, T. P. Lehnert, M. Juckel, N. H. Menzler, A. Weber, *Fuel Cells* **2023**, *23*, 430.
[7] A. Nakajo, A. P. Cocco, M. DeGostin, P. Burdet, A. A. Peracchio, B. N. Cassenti, M. Cantoni, W. K. Chiu, et al., *ECS Trans.* **2017**, *78*, 3205.
[8] H.-Y. Chen, H.-C. Yu, J. S. Cronin, J. R. Wilson, S. A. Barnett, K. Thornton, *J. Power Sources* **2011**, *196*, 1333.
[9] Q. Li, L. Liang, K. Gerdes, L.-Q. Chen, *Appl. Phys. Lett.* **2012**, *101*, 3.
[10] F. Abdeljawad, B. Völker, R. Davis, R. M. McMeeking, M. Haataja, *J. Power Sources* **2014**, *250*, 319.
[11] Z. Jiao, N. Shikazono, *J. Power Sources* **2016**, *305*, 10.
[12] Y. Lei, T.-L. Cheng, H. Abernathy, W. Epting, T. Kalapos, G. Hackett, Y. Wen, *J. Power Sources* **2021**, *482*, 228971.
[13] Y. Wang, C. Wu, Q. Du, M. Ni, K. Jiao, B. Zu, *Applications in Energy and Combustion Science* **2021**, *5*, 100016.
[14] S. Yang, J. Gao, M. Trini, S. De Angelis, P. S. Jørgensen, J. R. Bowen, L. Zhang, M. Chen, *Acta Mater.* **2023**, *246*, 118708.
[15] A. Choudhury, B. Nestler, *Phys. Rev. E* **2012**, *85*, 021602.
[16] P. W. Hoffrogge, A. Mukherjee, E. Nani, P. K. Amos, F. Wang, D. Schneider, B. Nestler, *Phys. Rev. E* **2021**, *103*, 033307.
[17] P. W. Hoffrogge, D. Schneider, F. Wankmüller, M. Meffert, D. Gerthsen, A. Weber, B. Nestler, M. Wieler, *J. Power Sources* **2023**, *570*, 233031.
[18] P. Haremski, L. Epple, M. Wieler, P. Lupetin, R. Thelen, M. J. Hoffmann, *Acta Mater.* **2021**, *214*, 116936.
[19] P. Haremski, L. Epple, M. Wieler, P. Lupetin, L. Klinger, E. Rabkin, M. J. Hoffmann, *Acta Mater.* **2022**, *241*, 118334.
[20] A. Koeppe, F. Bamer, M. Selzer, B. Nestler, B. Markert, *PAMM* **2021**, *21*, e202100238.
[21] B. Settles, (**2009**). *Active learning literature survey*, Computer Sciences Technical Report, 1648 University of Wisconsin-Madison.
[22] P. I. Frazier, A tutorial on bayesian optimization, *arXiv preprint arXiv:1807.02811* **2018**.
[23] Q. Liang, A. E. Gongora, Z. Ren, A. Tiihonen, Z. Liu, S. Sun, J. R. Deneault, D. Bash, F. Mekki-Berrada, S. A. Khan, K. Hippalgaonkar, B. Maruyama, K. A. Brown, J. Fisher, T. Buonassisi, *npj Comput. Mater.* **2021**, *7*, 188.
[24] G. Tosato, A. Koeppe, M. Selzer, B. Nestler, *Tage 2023* **2023**, 306.
[25] R. Roussel, J. P. Gonzalez-Aguilera, Y.-K. Kim, E. Wisniewski, W. Liu, P. Piot, J. Power, A. Hanuka, A. Edelen, *Nat. Commun.* **2021**, *12*, 5612.
[26] F. Ji, A. Edelen, R. Roussel, X. Shen, S. Miskovich, S. Weathersby, D. Luo, M. Mo, P. Kramer, C. Mayes, M. A. K. Othman, E. Nanni, X. Wang, A. Reid, M. Minitti, R. J. England, *Nat. Commun.* **2024**, *15*, 4726.
[27] F. Rahmanian, M. Vogler, C. Wölke, P. Yan, M. Winter, I. Cekic-Laskovic, H. S. Stein, *Batteries & Supercaps* **2022**, *5*, e202200228.
[28] M. E. Günay, N. A. Tapan, *J. Appl. Electrochem.* **2023**, *53*, 415.
[29] N. A. Tapan, *Chemom. Intell. Lab. Syst.* **2022**, *230*, 104677.
[30] Y. Zhao, P. Altschuh, J. Santoki, L. Griem, G. Tosato, M. Selzer, A. Koeppe, B. Nestler, *Acta Mater.* **2023**, *253*, 118922.
[31] R. Kulagin, P. Reiser, K. Truskovskyi, A. Koeppe, Y. Beygelzimer, Y. Estrin, P. Friederich, P. Gumbsch, *Adv. Eng. Mater.* **2023**, *25*, 2300048.
[32] Y. Zhao, N. Schiffmann, A. Koeppe, N. Brandt, E. C. Bucharsky, K. G. Schell, M. Selzer, B. Nestler, *Front. Mater.* **2022**, *9*, 821817.
[33] B. Lei, T. Q. Kirk, A. Bhattacharya, D. Pati, X. Qian, R. Arroyave, B. K. Mallick, *npj Comput. Mater.* **2021**, *7*, 194.
[34] L. C. Melo, P. Tigas, A. Abate, Y. Gal, Deep bayesian active learning for preference modeling in large language models, **2024**.
[35] A. Koeppe, The KadiAI Team, Cids: 3.1.
[36] N. Brandt, L. Griem, C. Herrmann, E. Schoof, G. Tosato, Y. Zhao, P. Zschumme, M. Selzer, *Data Sci. J.* **2021**, *20*, 8.
[37] B. Nestler, H. Garcke, B. Stinner, *Phys. Rev. E: Stat. Nonlinear Soft Matter Phys.* **2005**, *71*, 041609.
[38] I. Steinbach, F. Pezzolla, *Physica D* **1999**, *134*, 385.
[39] A. Sciazko, T. Shimura, Y. Komatsu, N. Shikazono, *J. Therm. Sci. Technol.* **2021**, *16*, JTST0013.
[40] M. Seiz, P. Hoffrogge, H. Hierl, A. Reiter, D. Schneider, B. Nestler, in *High Performance Computing in Science and Engineering'20: Transactions of the High Performance Computing Center, Stuttgart (HLRS) 2020*. Springer, **2021**, pp. 561–577.
[41] J. Blakely, H. Mykura, *Acta Metall.* **1961**, *9*, 23.
[42] P. Maiya, J. Blakely, *J. Appl. Phys.* **1967**, *38*, 698.
[43] J. R. Wolfe, *Surface self-diffusion on nickel (111) by radioactive tracers*, (**1968**). Doctoral Dissertations, https://scholarsmine.mst.edu/doctoral_dissertations/2283.
[44] E. Latta, H. Bonzel, *Phys. Rev. Lett.* **1977**, *38*, 839.
[45] T. Roth, *Mater. Sci. Eng.* **1975**, *18*, 183.

[46] E. Hayward, A. Greenough, *J. Inst. Met.* **1959**, *88*, 217.
[47] R. Digilov, S. Zadumkin, V. Kumykov, K. B. Khokonov, *Fiz. Met. Metalloved.;(USSR)* **1976**, *41*, 5.
[48] E. Clark, R. Yeske, H. Birnbaum, *Metall. Trans. A* **1980**, *11*, 1903.
[49] D. Stickle, J. Hirth, G. Meyrick, R. Speiser, *Metall. Trans. A* **1976**, *7*, 71.
[50] R. Tran, Z. Xu, B. Radhakrishnan, D. Winston, W. Sun, K. A. Persson, S. P. Ong, *Sci. Data* **2016**, *3*, 1.
[51] M. Kappeler, A. Marusczyk, B. Ziebarth, *Materialia* **2020**, *12*, 100675.
[52] R. Fujimatsu, T. Oda, M. Kobayashi, H. Ohka, M. Izumi, *ECS Trans.* **2016**, *71*, 113.
[53] A. T. Hasouna, K. Nogi, K. Ogino, *Mater. Trans., JIM* **1990**, *31*, 302.
[54] K. Mukai, Z. Yuan, K. Nogi, T. Hibiya, *ISIJ Int.* **2000**, *40*, S148.
[55] N. Zouvelou, X. Mantzouris, P. Nikolopoulos, *Mater. Sci. Eng., A* **2008**, *495*, 54.
[56] M. Jn, E. Shimada, Y. Ikuma, *J. Ceram. Soc. Jpn.* **2000**, *108*, 456.
[57] A. R. Symington, M. Molinari, S. Moxon, J. M. Flitcroft, D. C. Sayle, S. C. Parker, *J. Phys. Chem. C* **2020**, *124*, 3577.
[58] N. Skorodumova, M. Baudin, K. Hermansson, *Phys. Rev. B* **2004**, *69*, 075401.
[59] M. Nolan, S. C. Parker, G. W. Watson, *Surf. Sci.* **2005**, *595*, 223.
[60] H. Nahor, H. Meltzman, W. D. Kaplan, *J. Mater. Sci.* **2014**, *49*, 3943.
[61] H. Nahor, W. D. Kaplan, *J. Am. Ceram. Soc.* **2019**, *102*, 2987.
[62] B. Münch, L. Holzer, *J. Am. Ceram. Soc.* **2008**, *91*, 4059.
[63] J. Joos, T. Carraro, A. Weber, E. Ivers-Tiffée, *J. Power Sources* **2011**, *196*, 7302.
[64] K. Palágyi, A. Kuba, *Pattern Recognit. Lett.* **1998**, *19*, 613.
[65] J. Joos, *Microstructural characterisation, modelling and simulation of solid oxide fuel cell cathodes*, vol. *30*, KIT Scientific Publishing, Karlsruhe, **2017**.
[66] L. Griem, P. Zschumme, M. Laqua, N. Brandt, E. Schoof, P. Altschuh, M. Selzer, *Data Sci. J.* **2022**, *21*, 16.
[67] F. Chollet, et al., Keras, **2015**, https://github.com/fchollet/keras.
[68] F. Pedregosa, G. Varoquaux, A. Gramfort, V. Michel, B. Thirion, O. Grisel, M. Blondel, P. Prettenhofer, R. Weiss, V. Dubourg, J. Vanderplas, A. Passos, D. Cournapeau, M. Brucher, M. Perrot, E. Duchesnay, *J. Mach. Learn. Res.* **2011**, *12*, 2825.
[69] C. E. Rasmussen, C. K. I. Williams, *Gaussian Processes for Machine Learning*, **2006**, *2*, MIT Press Cambridge, MA.
[70] J. Snoek, H. Larochelle, R. P. Adams, *Adv. Neural. Inf. Process. Syst.* **2012**, *25*.
[71] C. Hvarfner, E. O. Hellsten, L. Nardi, *arXiv preprint arXiv:2402.02229* **2024**.
[72] X. Lin, Z. Yang, X. Zhang, Q. Zhang, *Adv. Neural. Inf. Process. Syst.* **2022**, *35*, 19231.
[73] A. Messac, G. J. Sundararaj, R. V. Tappeta, J. E. Renaud, *AIAA J.* **2000**, *38*, 1084.
[74] M. Ehrgott, *Multicriteria optimization*, **2005** Springer-Verlag, Berlin, Heidelberg.
[75] C. Bazgan, S. Ruzika, C. Thielen, D. Vanderpooten, *Theory of Computing Systems* **2022**, 1.
[76] Z. Jiao, E. P. Busso, N. Shikazono, *J. Electrochem. Soc.* **2020**, *167*, 024516.
[77] G. Lan, J. M. Tomczak, D. M. Roijers, A. Eiben, *Swarm Evol. Comput.* **2022**, *69*, 100970.
[78] R. Cheng, C. He, Y. Jin, X. Yao, *Complex Intell. Syst.* **2018**, *4*, 283.
[79] J. Hötzer, A. Reiter, H. Hierl, P. Steinmetz, M. Selzer, B. Nestler, *J. Comput. Sci.* **2018**, *26*, 1.
[80] G. Tosato, *Zenodo*, https://doi.org/10.5281/zenodo.14945900, **2025**.